

1 Regional-scale paleofluid system across the Tuscan Nappe - Umbria Marche Apennine Ridge (northern
2 Apennines) as revealed by mesostructural and isotopic analyses of stylolite-vein networks

3 Nicolas Beaudoin^{1,*}, Aurélie Labeur^{1,2}, Olivier Lacombe², Daniel Koehn³, Andrea Billi⁴, Guilhem
4 Hoareau¹, Adrian Boyce⁵, Cédric M. John⁷, Marta Marchegiano⁷, Nick M. Roberts⁶, Ian L. Millar⁶, Fanny
5 Claverie⁸, Christophe Pecheyran⁸, and Jean-Paul Callot¹.

6 1. Université de Pau et des Pays de l'Adour, E2S UPPA, LFCR, Pau, France
7 (nicolas.beaudoin@univ-pau.fr)

8 2. Sorbonne Université, CNRS-INSU, Institut des Sciences de la Terre de Paris - ISTeP, Paris,
9 France

10 3. GeoZentrum Nordbayern, University Erlangen-Nuremberg, Erlangen, Germany

11 4. Consiglio Nazionale delle Ricerche, Roma, Italy

12 5. Scottish Universities Environmental Research Centre (SUERC), East Killbride, UK

13 6. Geochronology and Tracers Facility, British Geological Survey, Environmental Science Centre,
14 Nottingham, NG12 5GG, UK

15 7. Department of Earth Sciences & Engineering, Imperial College London, London, UK

16 8. Université de Pau et des Pays de l'Adour, E2S UPPA, IPREM, Pau, France

17 Abstract

18 We report the results of a multi-proxy study that combines structural analysis of a fracture-stylolite
19 network and isotopic characterization of calcite vein cements/fault coating. Together with new
20 paleopiezometric and radiometric constraints on burial evolution and deformation timing, these
21 results provide a first-order picture of the regional fluid systems and pathways that were present
22 during the main stages of contraction in the Tuscan Nappe and Umbria Marche apennine ridge
23 (Northern Apennines). We reconstruct four steps of deformation at the scale of the belt: burial-related
24 stylolitization, Apenninic-related layer-parallel shortening with a contraction trending NE-SW, local
25 extension related to folding and late stage fold tightening under a contraction still striking NE-SW. We
26 combine the paleopiezometric inversion of the roughness of sedimentary stylolites - that constrains
27 the range of burial depth of strata prior to layer-parallel shortening - with burial models and U-Pb
28 absolute dating of fault coatings in order to determine the timing of development of mesostructures.
29 In the western part of the ridge, layer-parallel shortening started in Langhian time (~15 Ma), then
30 folding started at Tortonian time (~8 Ma), late stage fold tightening had started by the early Pliocene
31 (~5 Ma) and likely lasted until recent/modern extension occurred (~3 Ma onward). The textural and
32 geochemical ($\delta^{18}\text{O}$, $\delta^{13}\text{C}$, $\Delta_{47}\text{CO}_2$ and $^{87}\text{Sr}/^{86}\text{Sr}$) study of calcite vein cements and fault coatings reveals
33 that most of the fluids involved in the belt during deformation are either local or flowed laterally from
34 the same reservoir. However, the western edge of the ridge recorded pulses of eastward squeegee-
35 type migration of hydrothermal fluids (>140°C), that can be related to the difference in structural style
36 of the subsurface between the eastern Tuscan Nappe and the Umbria Marche Ridge.

37 Introduction

38 The upper crust is the locus of omnipresent fluid migrations that occur at all scales, leading to
39 strain localization, earthquake triggering and georesource generation, distribution and storage (e.g.,
40 Cartwright, 2007; Andresen, 2012; Bjørlykke, 1994, 1993; Lacombe and Rolland, 2016; Lacombe et al.,
41 2014; Roure et al., 2005; Agosta et al., 2016). Carbonate rocks host an important part of the world's
42 exploited hydrocarbons, strategic ores and water resources (Agosta et al., 2010). It is thus a

43 fundamental topic to depict the history of fluid migration in deformed carbonates. Such knowledge
44 impacts both the prediction and monitoring of energy prospect and potential storage area, but also
45 may help refine our understanding of what mechanisms facilitate fluid migrations during diagenesis
46 of the sedimentary rocks, along with the time and spatial scales of fluid flow.

47 Fluid migration events and related accumulations are usually linked to past tectonic events,
48 especially to the large-scale faults and fracture networks created during these tectonic events. Indeed,
49 structural studies established that fracture networks in folded reservoirs are not exclusively related to
50 the local folding history (Stearns and Friedman, 1972), and can also be influenced by burial history
51 (Becker et al., 2010; Laubach et al., 2010; Laubach et al., 2019), and long-term and large-scale regional
52 deformation (Lacombe et al., 2011; Quintà and Tavani, 2012; Tavani and Cifelli, 2010; Tavani et al.,
53 2015; Bellahsen et al., 2006; Bergbauer and Pollard, 2004; Ahmadhadi et al., 2008; Sassi et al., 2012;
54 Beaudoin et al., 2012; Amrouch et al., 2010). In fold-and-thrust belts and orogenic forelands, it is for
55 example possible to subdivide the mesoscale deformation (faults, veins, stylolites) history into specific
56 stages (Tavani et al., 2015): extension related to foreland flexure and bulging; pre-folding layer-parallel
57 shortening (kinematically unrelated with folding); early folding layer-parallel shortening; syn-folding,
58 strata curvature-related, local extension; late stage fold tightening, the last three stages being
59 kinematically related with folding; and post-folding contraction or extension (kinematically unrelated
60 with folding).

61 In the past decades, a significant volume of work has been conducted in order to reconstruct past
62 fluid migrations through either localized fault systems or distributed sub-seismic fracture networks, in
63 relation with past tectonic events, from the scale of a single fold to that of the basin itself (Engelder,
64 1984; Reynolds and Lister, 1987; McCaig, 1988; Evans et al., 2010; Evans and Hobbs, 2003; Evans and
65 Fischer, 2012; Forster and Evans, 1991; Cruset et al., 2018; Lacroix et al., 2011; Travé et al., 2000; Travé
66 et al., 2007; Bjørlykke, 2010; Callot et al., 2017a; Callot et al., 2017b; Roure et al., 2010; Roure et al.,
67 2005; Van Geet et al., 2002; Vandeginste et al., 2012; Vilasi et al., 2009; Barbier et al., 2012; Beaudoin
68 et al., 2011; Beaudoin et al., 2014; Beaudoin et al., 2013; Beaudoin et al., 2015; Fischer et al., 2009;
69 Lefticariu et al., 2005; Di Naccio et al., 2005). A variety of fluid system evolution arises from published
70 studies, and it is established that fracture networks and related mineralization can witness long term
71 fluid migration in folded reservoirs. In some cases, fluid migration is stratigraphically
72 compartmentalized and directed by compressive tectonic stress. In other cases, mineralization record
73 an infill of meteoric fluids flowing downward, or of hydrothermal fluids (*i.e.* hotter than the host-rock
74 they precipitated in) flowing upward either from the basin or the basement rocks through large scale
75 faults or décollement levels (Roure et al., 2005; Vandeginste et al., 2012; Cruset et al., 2018; Lacroix
76 et al., 2011; Travé et al., 2000; Travé et al., 2007; De Graaf et al., 2019; Callot et al., 2010; Beaudoin et
77 al., 2014; Bertotti et al., 2017; Gonzalez et al., 2013; Lucca et al., 2019; Mozafari et al., 2019; Storti et
78 al., 2018; Vannucchi et al., 2010).

79 This contribution reports an orogen-scale paleofluid flow study in the Northern Apennine (Italy).
80 The study builds upon the mesostructural and geochemical analysis of vein and stylolite networks
81 within the competent Jurassic-Oligocene carbonate platform along a transect running across the
82 Tuscan Nappe (TN) and the Umbria-Marche Apennine Ridge (UMAR) (Fig. 1a). The data collection was
83 organized to cover a large area comprising several folds in order to be able to differentiate regional
84 trends from local, fold-related ones. We focused on identifying and characterizing the first order
85 pattern of mesostructures – faults, fractures and stylolites – associated with Layer-Parallel Shortening

86 (LPS) and with thrust-related folding, along with the isotopic measurements ($\delta^{18}\text{O}$, $\delta^{13}\text{C}$, $^{87}\text{Sr}/^{86}\text{Sr}$),
87 clumped isotope measurements ($\Delta_{47}\text{CO}_2$), and U-Pb absolute dating of their calcite cements. Without
88 an appraisal of which fracture trends are relevant to the large scale (*i.e.*, regional) tectonic evolution,
89 there is a risk to otherwise capture mesostructural and geochemical signals of local meaning only. In
90 order to discuss the local versus hydrothermal fluid origin, we also reconstructed burial curves using
91 strata thickness we correct from physical and chemical compaction. Novel constraints are added to
92 the timing and minimal depth of LPS-related deformation based on the study of the roughness of
93 bedding-parallel stylolites, the inversion of which reliably returns the maximum depth at which
94 compaction under a vertical maximum principal stress was prevailing in the strata. U-Pb absolute
95 dating of calcite steps on mesoscale faults further constrains the timing of folding. Such a multi-proxy
96 approach, that combines structural analysis of fracture-stylolite network and isotopic characterization
97 of cements, together with new constraints on burial evolution and deformation timing, provides a
98 picture of the regional fluid pathways during the Apenninic contraction.

100 1. Geological setting

101 The Neogene-to-Quaternary Apennines fold-and-thrust belt results from the convergence of
102 Eurasia and Africa (Lavecchia, 1988; Elter et al., 2012). It is associated with the eastward retreating
103 subduction of the Adriatic Plate under the European plate. The Apennines extend from the Po Plain
104 to the Calabrian arc, and are divided into two main arcs, the Northern Apennines that extend down to
105 the south of the UMAR, and the Southern Apennines that cover the remaining area down to the
106 Calabrian arc (Carminati et al., 2010). The evolution of the Apennines is characterized by a roughly
107 eastward migration of thrust fronts and associated foredeep basins, superimposed by post-orogenic
108 extension at the rear of the eastward propagating orogenic belt (Cello et al., 1997; Tavani et al., 2012;
109 Lavecchia, 1988; Ghisetti and Vezzani, 2002).

110 The study area, the Tuscan Nappe and the Umbria-Marches Apennines Ridge, comprises of a
111 succession of carbonate rocks, Upper Triassic to Oligocene in age, which corresponds to a carbonate
112 platform (Lavecchia, 1988; Carminati et al., 2010). The Umbrian carbonate units overlie early Triassic
113 evaporites that act as a décollement level, and that are themselves unconformably overlying the
114 crystalline basement rocks (Fig. 1b). Above the platform, Miocene turbidite deposits witness the
115 progressive eastward involvement of the platform into the fold-and-thrust belt (Calamita et al., 1994).
116 In the western part of the area, the belt is a thin-skinned assembly of piggy-back duplex folds (Fig. 1c),
117 the so-called Tuscan Nappe (TN), the folding and thrusting of which started by the late Aquitanian (*ca.*
118 23 - 20.43 Ma) and lasted until the Langhian (*ca.* 16 Ma to 13.8 Ma; Carboni et al., 2020). The UMAR
119 is an arcuate ridge exhibiting an eastward convex shape, with a line connecting Perugia and Ancona
120 separating a northern part where structural trends are oriented NW-SE, from a southern part where
121 structure trends are oriented N-S (Calamita and Deiana, 1988). Burial models suggest that, from
122 Burdigalian to early Messinian times, the TN was further buried under the allochthonous Ligurian
123 thrust sheet, reaching locally up to 1 km in thickness (Caricchi et al., 2015). In the eastern part (now
124 UMAR), the foreland was progressively folded and thrustured from the Lower Miocene in the
125 westernmost part of the current ridge to the Messinian in the foreland of the ridge (Mazzoli et al.,
126 2002). UMAR was considered a thin-skinned thrust belt where shortening was accommodated by
127 stacking and duplexing of sedimentary units detached above a décollement level located in the Triassic
128 evaporites (Conti and Gelmini, 1994; Carboni et al., 2020). The seismic profile of the CROsta Profonda
129 (CROP) project led authors to interpret the UMAR as resulting from thick-skinned tectonics, where the

130 basement is involved in shortening (Barchi et al., 1998) through the positive inversion of normal faults
131 inherited from the Jurassic Tethyan rifting (Fig. 1c). Even if the interpretation of basement-involved
132 shortening is more accepted now, the subsurface geometry is still debated, with some models
133 involving shallow duplexes (Tavarnelli et al., 2004; Mirabella et al., 2008), while in more recent works
134 surface folds are rather interpreted as related to high angle thrusts that either sole within the mid-
135 Triassic décollement, or involve the basement (Scisciani et al., 2014; Scisciani et al., 2019; Butler et al.,
136 2004)(Fig. 1c). For the latter interpretations, the style of deformation of the UMAR strongly contrasts
137 with the style of deformation of the TN where shortening is accommodated by allochthonous, far-
138 travelled duplex nappes (Carboni et al., 2020)(Fig. 1c). The cross-section of Figure 1c also implies that
139 at least part of the motion on the décollement level at the base of the TN postdates the westernmost
140 activation of steep thrusts of the UMAR, as the thrust at the base of the TN cuts and offsets the west-
141 verging basement fault in the area of Monte Subasio. Currently, the whole TN-UMAR area is
142 experiencing extension, with numerous active normal faults developing trenches, as the contraction
143 front migrated toward the Adriatic Sea (d'Agostino et al., 2001).

144 Our sampling focused on the carbonate formations cropping out from W to E in the Cetona area
145 located west from Perugia; the Monte Corona in the TN; the Monte Subasio, Gubbio Area, Spolelto
146 Area, Monte Nero, Monte Catria, Monte San Vicino, and Monte Cingoli in the UMAR, and the Monte
147 Conero, the youngest onshore anticline related to the Apenninic compression, located on the coast
148 line (Fig. 1a). The sampled units comprise, following the stratigraphic order (Fig. 1b): the Triassic
149 anhydrites and dolostones of the Anidridi di Burano Formation focusing on the limestone and marl
150 intercalation at the top; (2) Liassic massive dolomites of the Calcare Massiccio Fm. (Hettangian to
151 Sinemurian, *ca.* 203-195 Ma); (3) the grey Jurassic limestones with chert beds of the Corniola Fm.
152 (Sinemurian-Pleisbachian, *ca.* 195-184 Ma); (4) the micritic limestones, marls, and cherts of the
153 Calcare Diasprini Fm (Bajocian-Tithonian, *ca.* 160-140 Ma); (5) the white limestones with chert beds
154 of the Maiolica Fm. (Tithonian-Aptian, *ca.* 140-110 Ma); (6) the marly limestones of the Fucoidi Fm.
155 (Aptian-Albian, *ca.* 110-100 Ma); (7) the white marly limestones of the Scaglia Bianca Fm. (Albian-
156 Turonian, *ca.* 100-90 Ma); (8) the pink marly limestones of the Scaglia Rossa Fm. (Turonian-Priabonian,
157 *ca.* 90 – 37 Ma); and (9) the grey marly limestones of the Scaglia Cinerea Fm. (Priabonian- Aquitanian,
158 *ca.* 37- 21 Ma). Up to 3000m of Miocene turbidites were deposited when the area of interest was the
159 foredeep ahead of the advancing fold-and-thrust belt and during fold development, including clay-rich
160 limestones and silts of Marnoso-Aranacea (Aquitanian-Tortonian, *ca.* 21-7 Ma); in the eastern part of
161 the ridge (east of the Cingoli anticline), thicker foredeep deposits are Messinian to Pliocene (*ca.* 7 to
162 3 Ma) in age.

163

164 2. Methods

165 The approach adopted relies on structural and geochemical analyses the results of which are
166 combined to establish a scenario of fluid flow and fluid-rock interaction during deformation of the
167 Umbria-Marche Apennine Ridge in the Northern Apennines.

168 a. Mesostructural analysis of joints, veins and striated fault planes

169 ~1300 joint and vein orientations, along with tectonic stylolite orientations, were measured
170 along a WSW-ENE transect going from Cetona in the TN to Monte Conero on the coastline (Fig. 1a).
171 For each measurement site, fractures and tectonic stylolites (*i.e.* bedding perpendicular dissolution

172 planes displaying horizontal peaks after unfolding or vertical dissolution planes displaying horizontal
 173 peaks in the current bed attitude) were measured. Chronological relationships between
 174 mesostructures were carefully observed in the field (Fig. 2) and checked in thin sections under the
 175 optical microscope when possible (Fig. 3). Poles to fractures and stylolite peaks were projected on
 176 Schmidt stereograms, lower hemisphere, in the current attitude of the strata (Raw), and after
 177 unfolding (Unfolded) (Fig. 4). Assuming the same mode of deformation (*i.e.* mode I opening) and
 178 consistent chronological relationships and orientation, we use Fisher density to define statistically
 179 meaningful sets of joints/veins. Tectonic stylolite planes and peaks were measured, and we consider
 180 that the average orientation of the stylolite peaks at the fold scale represents the orientation of the
 181 horizontal maximum principal stress (σ_1), as peaks grow parallel to the main shortening direction. To
 182 complement this mesostructural analysis, striated fault planes were measured (1) in the Langhian
 183 carbonates from the Camerino syncline West from Monte San Vicino, and (2) in the forelimb of the
 184 Monte Subasio, with one site in the Scaglia Cinerea and one site in the Scaglia Rossa e Bianca. At each
 185 site, paleostress orientations (local trend and plunge) and regimes (reverse, extensional, strike-slip)
 186 were calculated using inversion techniques (Angelier, 1984). Published studies in the UMAR highlight
 187 the complexity of fracture patterns at the fold scale, that witness several phases of stress perturbation
 188 and stress/block rotation due to the local tectonics and structural inheritance (Tavani et al., 2008;
 189 Petracchini et al., 2012; Beaudoin et al., 2016; Díaz General et al., 2015). In order to capture the
 190 mesostructural and fluid flow evolution at the regional scale during layer-parallel shortening and
 191 folding, we gathered the statistically most representative fracture data by structure, regardless of the
 192 structural complexity in the individual folds, and corrected them from the local bedding dip using an
 193 opensource stereodiagram rotation program (Grohmann and Campanha, 2010) to discriminate
 194 between early and syn-folding features.

195 b. Inversion of sedimentary stylolites

196 Bedding-parallel stylolites are rough dissolution surfaces that developed in carbonates in flat
 197 laying strata during burial at the time when σ_1 was vertical. As proposed by Schmittbuhl et al. (2004)
 198 and later developed by Koehn et al. (2012), Ebner et al. (2009b); Ebner et al. (2010), Rolland et al.
 199 (2014) and Beaudoin et al. (2019); Beaudoin et al. (2020), the 1-D roughness of a track along the
 200 bedding-parallel stylolite (*i.e.* difference in height between two points along the track) results from a
 201 competition between roughening forces (*i.e.* pining on non-soluble particles in the rocks) and
 202 smoothing forces (*i.e.* the surface energy at scale typically < 1mm, and the elastic energy at scale >
 203 1mm). The stylolite growth model (Koehn et al., 2007; Ebner et al., 2009a; Rolland et al., 2012;
 204 Toussaint et al., 2018) predicts that the surface energy-controlled scale returns a steep slope
 205 characterized by a roughness exponent (so-called Hurst exponent) of 1.1 ± 0.1 , while the elastic
 206 energy-controlled scale returns a gentle slope with a roughness exponent of 0.5 to 0.6 (Fig. 5). The
 207 length at which the change in roughness exponent occurs, called the cross-over length (L_c , in mm), is
 208 directly related to the magnitude of differential and mean stress ($\sigma_d = \sigma_1 - \sigma_3$ and $\sigma_m = \frac{\sigma_1 + \sigma_2 + \sigma_3}{3}$,
 209 respectively, in Pa) prevailing in the strata at the time the stylolite stopped to be an active dissolution
 210 surface following:

$$211 \quad L_c = \frac{\gamma E}{\beta \sigma_m \sigma_d} \quad (1)$$

212 where E is the Young modulus of the rock (in Pa), γ is the solid-fluid interfacial energy (in $J.m^{-2}$), and
 213 $\beta = \nu(1-2\nu)/\pi$, a dimensionless constant with ν being the Poisson ratio. Samples of bedding parallel

214 stylolites of which peaks were perpendicular to the dissolution plane were collected in specific points
215 of the study area, and several stylolites were inverted. The inversion process follows the method
216 described in Ebner et al. (2009b). Samples were cut perpendicular to the stylolite, hand polished to
217 enhance the visibility of the track while being cautious to not altering the peaks, scanned at high-
218 resolution (12800 pixel per inches), and the 1D track was hand drawn with a pixel-based software
219 (GIMP). Each track was analyzed as a periodic signal by using the Average Wavelet Spectrum with
220 Daubechies D4 wavelets (Fig. 5) (Ebner et al., 2009b; Simonsen et al., 1998). In the case of bedding
221 parallel stylolites related to compaction and burial, we assume the horizontal stress is isotropic in all
222 direction ($\sigma_v > \sigma_h = \sigma_h$) to simplify equation 1 (Schmittbuhl et al., 2004) as:

$$223 \quad \sigma_v^2 = \frac{\gamma E}{\alpha L c} \quad (2)$$

224 with

$$225 \quad \alpha = \frac{(1-2\nu)*(1+\nu)^2}{30\pi(1-\nu)^2} \quad (3)$$

226

227 According to the sampled formation, we used the solid-fluid interfacial energy γ of 0.24 J.m⁻²
228 for dolomite, and of 0.32 J.m⁻² for calcite (Wright et al., 2001). As an approximation for the material
229 mechanical properties, we use a Poisson ratio of $\nu=0.25 \pm 0.05$, and the average Young modulus
230 derived from the Jurassic-Eocene competent core of $E=24.2$ GPa (Beaudoin et al., 2016). It is important
231 to note that because of the non-linear regression method we use, and because of uncertainty on the
232 mechanical parameters of the rock at the time it dissolved, the uncertainty on the stress has been
233 calculated to be about 12% (Rolland et al., 2014). As the dissolution occurs along a fluidic film (Koehn
234 et al., 2012; Rolland et al., 2012; Toussaint et al., 2018), the stylolite roughness is unaffected by local
235 fluid overpressure until the system is fluidized and hydro-fractures (Vass et al., 2014), meaning it is
236 possible to translate vertical stress magnitude directly into depth if considering an average dry rock
237 density for clastic/carbonated sediments (2400 g.m⁻³, Manger (1963)), without any additional
238 assumption on the past thermal gradient or fluid pressure (Beaudoin and Lacombe, 2018). This
239 technique has already provided meaningful results in various settings (Bertotti et al., 2017; Rolland et
240 al., 2014; Beaudoin et al., 2019; Beaudoin et al., 2020).

241 Sedimentary stylolites also yield quantitative information on the volume of dissolved rocks
242 during burial (Toussaint et al., 2018), the minimum of which can be approached in 1D by measuring
243 the amplitude of the highest peak along the stylolite track (Table 1), and multiplying this height value
244 (in m) by the average density of stylolites (#/m) derived from field spacing measurement (Fig. 2 c-d, in
245 m).

246

247 c. O, C stable isotopes

248 Calcite cements in tectonic veins related either to layer-parallel shortening or to strata
249 curvature at fold hinges were studied petrographically (Fig. 3). The vein textures were characterized
250 in thin sections under an optical microscope, and possible post-cementation diagenesis such as
251 dissolution or replacement were checked under cathodoluminescence, using a cathodoluminescence
252 CITL CCL 8200 Mk4 operating under constant gun condition of 15kV and 300 μ A. To perform oxygen
253 and carbon stable isotope analysis on the cements that were the most likely to witness the conditions
254 of fluid precipitation at the time the veins opened, we selected those veins that (1) show no obvious

255 evidence of shear; (2) the texture of which was elongated blocky or fibrous (Fig. 3); and (3) show
256 homogeneous cement under cathodoluminescence (Fig. 3), precluding any later diagenetic alteration.

257 40 µg of calcite powder was hand sampled for each of 58 veins and 54 corresponding host-
258 rocks (sampled ~2 cm away from veins) in various structures and formation along the transect, in both
259 TN and UMAR. Carbon and oxygen stable isotopes were analyzed at the Scottish Universities
260 Environmental Research Centre (SUERC, East Kilbride, UK) on an Analytical Precision AP2003 dual inlet
261 mass spectrometer equipped with a separate acid injector system. As samples were either pure calcite
262 or pure dolomite, we placed samples in glass vials to conduct a reaction with 103% H₃PO₄ under a
263 helium atmosphere at 90°C, for 30 and 45 min on calcite and dolomite, respectively. Results are
264 reported in table 2, in permil relative to Vienna PeeDee Belemnite (‰ VPDB). Mean analytical
265 reproducibility based on replicates of the SUERC laboratory standard MAB-2 (Carrara Marble) was
266 around ± 0.2‰ for both carbon and oxygen. MAB-2 is an internal standard extracted from the same
267 Carrara Marble quarry, as is the IAEA-CO208 1 international standard. It is calibrated against IAEA-CO-
268 1 and NBS-19.

269 d. ⁸⁷Sr/⁸⁶Sr measurements

270 Sr-isotope analysis was performed at the Geochronology and Tracers Facility, British
271 Geological Survey. 2-10 mg of sample was weighed into 15ml Savillex teflon beakers and dissolved in
272 1-2mls of 10% Romil uPA acetic acid. After evaporating to dryness, the samples were converted to
273 chloride form using 2 ml of Teflon-distilled HCl. The samples were then dissolved in ca. 1 ml of
274 calibrated 2.5M HCl in preparation for column chemistry, and centrifuged. Samples were pipetted
275 onto quartz-glass columns containing 4mls of AG50x8 cation exchange resin. Matrix elements were
276 washed off the column using 48 ml of calibrated 2.5M HCl and discarded. Sr was collected in 12 ml of
277 2.5M HCl and evaporated to dryness.

278 Sr fractions were loaded onto outgassed single Re filaments using a TaO activator solution and
279 analyzed in a Thermo-Electron Triton mass spectrometer in multi-dynamic mode. Data are normalized
280 to ⁸⁶Sr/⁸⁸Sr = 0.1194. Three analyses of the NBS987 standard run with the samples gave a value of
281 0.710250 ± 0.000001 (1-sigma).

282 e. Carbonate clumped isotope paleothermometry (Δ₄₇ CO₂)

283 Clumped isotopes analyses were carried out in the Qatar Stable Isotope Laboratory at Imperial
284 College London. The technique relies on the tendency for heavy isotopes (¹³C, ¹⁸O) to ‘clump’ together
285 in the same carbonate molecule, that varies only by temperature. Since the clumping of heavy
286 isotopes within a molecule is a purely stochastic process at high temperature but is systematically
287 over-represented (relative to randomly distributing isotopes among molecules) at low temperature,
288 the ‘absolute’ temperature of carbonate precipitation can be constrained using clumped isotope
289 abundances.

290 The clumped isotopes laboratory methods at Imperial College follow the protocol of Dale et
291 al. (2014) as adapted for the automated clumped isotope measurement system IBEX (Imperial Batch
292 EXtraction) system (Cruset et al., 2016). Typical sample size was 3.5 mg of calcite powder per replicate.
293 Measurement of ¹³C-¹⁸O ordering in sample calcite was achieved by measurement of the relative
294 abundance of the ¹³C¹⁸O¹⁶O isotopologues (mass 47) in acid evolved CO₂ and is referred in this paper
295 as Δ₄₇ CO₂. A single run on the IBEX comprises 40 analyses, 30% of which are standards. Each analysis
296 takes about 2 hours. The process starts with 10 minutes of reaction of the carbonate powder in a

297 common acid bath containing 105% orthophosphoric acid at 90°C to liberate CO₂. The CO₂ gas is then
298 captured in a water/CO₂ trap maintained at liquid nitrogen temperature, and then moved through a
299 hydrocarbon trap filled with poropak and a second water trap using helium as carrier gas. At the end
300 of the cleaning process, the gas is transferred into a cold finger attached to the mass spectrometer,
301 and into the bellows of the mass spectrometer. Following transfer, analyte CO₂ was measured on a
302 dual inlet Thermo MAT 253 mass spectrometers (MS “Pinta”). The reference gas used is a high purity
303 CO₂, with the following reference values: -37.07‰ δ¹³C_{V_{PDB}}, 8.9‰ δ¹⁸O_{V_{S_{MOW}}}. Measurements comprise
304 8 acquisitions each with 7 cycles with 26s integration time. A typical acquisition time is 20 minutes,
305 corresponding to a total analysis time of 2 hours.

306 Data processing was carried out in the freely available stable isotope management software,
307 *Easotope* (www.easotope.org, John and Bowen, 2016). The raw Δ₄₇ CO₂ is corrected in three steps.
308 First, mass spectrometer non-linearity was corrected by applying a “pressure baseline correction”
309 (Bernasconi et al., 2013). Next, the Δ₄₇ results were projected in the absolute reference frame or
310 Carbon Dioxide Equilibrated Scale (CDES, Dennis et al., 2011) based on routinely measured ETH1,
311 ETH2, ETH3, ETH4 and Carrara Marble (ICM) carbonate standards (Meckler et al., 2014; Muller et al.,
312 2017). The last correction to the raw Δ₄₇ was to add an acid correction factor of 0.082‰ to obtain a
313 final Δ₄₇CO₂ value (Defliese et al., 2015). Temperatures of precipitation were then estimated using the
314 equation of Davies and John (2019). The bulk isotopic value of δ¹⁸O was corrected for acid digestion
315 at 90°C by multiplying the value by 1.0081 using the published fractionation factor valid for calcite
316 (Kim et al., 2007). Contamination was monitored by observing the values on mass 48 and 49 from each
317 measurement, using a Δ₄₈ offset value > 0.5‰ and/or a 49 parameter values > 0.3 as a threshold to
318 exclude individual replicates from the analysis (Davies and John, 2019).

319 f. U-Pb absolute dating of veins and faults

320 The calcite U-Pb geochronology was conducted in two different ways, of which specific methodology
321 is reported as supplementary material:

322 - LA-ICPMS trace elements and U-Pb isotope mapping were performed at the Geochronology and
323 Tracers Facility, British Geological Survey, UK, on 6 vein samples. Data were generated using a Nu
324 Instruments Attom single collector inductively coupled plasma mass spectrometer coupled to a
325 NWR193UC laser ablation system fitted with a TV2 cell, following protocol reported previously
326 (Roberts et al., 2017; Roberts and Walker, 2016). Laser parameters were 110 μm spots, ablated at 10
327 Hz for 30 seconds with a fluence of 7 J/cm². WC1 (Roberts et al., 2017) was used as a primary reference
328 material for Pb/U ratios, and NIST614 for Pb/Pb ratios; no secondary reference materials were run
329 during the session. Additional constraints on U-Pb composition were calculated from the Pb and U
330 masses measured during the trace element mapping. Baselines were subtracted in Iolite, and Pb/Pb
331 and Pb/U ratios were calculated offline in excel. No normalisation was conducted, as the raw ratios
332 are suitable accurate to assess

333 - LA-ICPMS U-Pb isotope mapping approach was undertaken at the Institut des Sciences Analytiques
334 et de Physico-Chimie pour l'Environnement et les Matériaux (IPREM) Laboratory (Pau, France). All the
335 29 samples were analysed with a 257 nm femtosecond laser ablation system (Lambda3, Nexeya,
336 Bordeaux, France) coupled to an HR-ICPMS Element XR (ThermoFisher Scientific, Bremen, Germany)
337 fitted with the Jet Interface (Donard et al., 2015). The method is based on the construction of isotopic
338 maps of the elements of interest for dating (U,Pb,Th) from ablation along lines, with ages calculated
339 from the pixel values (Hoareau et al., 2020). The ablation was made in a helium atmosphere (600 mL

340 min⁻¹), and 10 mL min⁻¹ of nitrogen was added to the helium flow before mixing with argon in the
341 ICPMS. Measured wash out time of the ablation cell was ~500 ms for helium gas. The fs-LA-ICP-MS
342 coupling was tuned daily, and the additional Ar carrier gas flow rate, torch position and power were
343 adjusted so that the U/Th ratio was close to 1 +/- 0.05 when ablating the glass SRM NIST612. Detector
344 cross-calibration and mass bias calibration were checked daily. The laser and HR-ICPMS parameters
345 used for U-Pb dating are detailed in the supplementary material.

346

347 3. Results

348 a. Mesostructural analysis of joints, veins and striated fault planes

349 Based on the average orientation and the angle to the local fold axis, we group veins/joints in
350 2 main sets labelled J (Fig. 4):

351 - set J1 comprises joints/veins at high angle to bedding, that strike E-W to NE-SW but
352 perpendicular to the local strike of fold axis. The trend of this set J1 evolves eastward as follows: E-W
353 in the westernmost part (Cetona, Subasio), E-W to NE-SW in the central part (Catria, Nero), NE-SW in
354 the eastern part of the chain (San Vicino, Cingoli), and ENE-WSW in the far foreland (Conero).

355 - set J2 comprises joints/veins at high angle to bedding that strike parallel to the local trend of
356 the fold hinge, *i.e.* NW-SE in the ridge to N-S in the outermost part of the belt, where the arcuate
357 shape is more marked.

358 Note that as set J1 strikes perpendicular to the local strata direction, it is impossible to infer a pre-,
359 syn- or post-tilting (post-tilting then called J3 hereinafter) origin for its development. In most case
360 though, abutment relationships establish a relative chronology with set J1 predating set J2 (Fig. 3).
361 The veins of sets J1 and J2 show twinned calcite grains (Fig 3) with mostly thin and rectilinear twins
362 (thickness < 5 µm, Fig. 3). Another set comprising joints striking N-S and oblique to the direction of the
363 fold axis is documented in the Monte Catria. It is also encountered at other locations but can be
364 regarded as a second order set at regional scale on a statistical basis. This set could be tentatively
365 related to lithospheric flexure (Mazzoli et al., 2002; Tavani et al., 2012), but as it is the least
366 represented in our data, it will not be considered hereinafter.

367

368 Most tectonic stylolites have peaks striking NE-SW (Fig. 4), but they can be split in two sets
369 labelled S based on the orientation of their planes with respect to the local bedding:

- 370 - Set S1 comprises bed-perpendicular, vertical stylolite planes containing horizontal peaks in
371 the unfolded attitude of strata;
- 372 - Set S2 comprises ~vertical stylolite planes containing ~horizontal peaks in the current attitude
373 of strata (set S2).

374 S1 and S2 are not always easily distinguished when both occurred at the fold scale because (1) stylolite
375 data were often collected in shallow dipping strata, (2) peaks are not always perpendicular to the
376 stylolite planes, and (3) the orientation data are scattered with intermediate plunges of the peaks.
377 Another set showing stylolite planes with N-S peaks parallel to bedding is documented at Monte
378 Subasio only, thus will not be considered in the regional sequence of deformation.

379 Finally, some mesoscale reverse and strike-slip conjugate fault systems have been measured
380 (sets labelled F), of which fault-slip data inversion under specific assumptions (e.g., Lacombe, 2012)
381 yields (1) a NE-SW contraction in the unfolded attitude of the strata (early folding set F1, flexural-slip
382 related, bedding-parallel reverse faults) and (2) a NE-SW contraction in the current attitude of the
383 strata (late folding set F2, strike-slip conjugate faults and reverse faults).

384

385 b. Inversion of sedimentary stylolites

386 The paleopiezometric study of 30 bedding-parallel stylolites returned a range of burial depths,
387 across the UMAR, from W to E, reported in table 1. Most data come from the western part of the
388 UMAR: in the Subasio Anticline (n=7), the depth returned by the Scaglia Bianca and the lower part of the
389 the Scaglia Rossa Fms. ranges from ca. 800 ± 100 m to ca. 1450 ± 150 m. In Fiastra area (n=6), the
390 depth returned for the Maiolica Fm. ranges from 800 ± 100 m to 1200 ± 150 m. In the Gubbio fault
391 area (n=4), the depth returned for the Jurassic Corniola Fm. ranging from 600 ± 70 m to 1450 ± 150 m.
392 In the Monte Nero (n=11), the depth data published by Beaudoin et al., (2016), and updated here
393 range from 750 ± 100 m to 1350 ± 150 m in the Maiolica. Fewer data comes from the western part of
394 the UMAR: in the Monte San Vicino (n=2), the depth returned for the Maiolica Fm. ranges from 1000
395 ± 100 m to 1050 ± 100 m. Finally, the depth reconstructed for the lower part of the Scaglia Rossa is
396 650 ± 70 m in the foreland at Conero Anticline (n=1). The maximum height of peaks along the studied
397 stylolite tracks ranges from 0.6 to 8.5 mm (n=30) with a mean value of 2.6 mm. Spacing values for
398 these stylolites were measured on outcrops (Fig. 2) and range from 1 to 2 cm, averaging the number
399 of stylolite per meter to 70. Considering that dissolution is isotropic along the stylolite plane, the
400 volume of rock loss in relation to the chemical compaction is 18%.

401

c. O, C stable isotopes

402 At the scale of the study area, most formations cropping out were sampled (Table 2), and
403 oxygen isotopic values of the vein cements and striated fault coatings range from -16.8‰ to 3.7‰
404 VPDB while in the host rocks values range from -5.3‰ to 0.4‰ VPDB. Carbon isotopic values range
405 from -9.7‰ to 2.7‰ VPDB, and from 0.0‰ to 3.5‰ VPDB in the veins and in the host rock,
406 respectively (Fig. 6a-b). Isotopic values are represented either according to the structure where they
407 have been sampled in, irrespective of the structural position in the structure (*i.e.* limbs or hinge), or
408 according to the set they belong to, differentiating the sets J1, J2 and F1 (Fig. 6a). At the scale of the
409 belt, isotopic values of host rocks are very similar, the only noteworthy point being that the Triassic
410 carbonates have lower $\delta^{18}\text{O}$ than the rest of the column ($\delta^{18}\text{O}$ of -5.5‰ to -3.5‰ versus -3.2‰ to $-$
411 1.0‰ VPDB, Fig. 6b). Considering the vein cements, the $\delta^{13}\text{C}$ values are rather similar in all structures
412 and in all sets, a vast majority of veins showing cements with values of $1.5 \pm 1.5\text{‰}$ VPDB. In most
413 structures, the $\delta^{13}\text{C}$ values of the veins are similar to the $\delta^{13}\text{C}$ values of the host rock, with the notable
414 exception of the veins hosted in Triassic carbonates of the Cetona anticline, where the shift between
415 $\delta^{13}\text{C}$ values of veins and $\delta^{13}\text{C}$ values of host rocks ranges from $+4.0\text{‰}$ VPDB to $+7.5\text{‰}$ VPDB (Fig. 6c).
416 The $\delta^{18}\text{O}$ values are ranging from -6.0‰ VPDB to $+3.7\text{‰}$ VPDB in most of the structures and formation,
417 irrespectively of vein set. However, veins sampled in Monte Subasio and Monte Corona return very
418 negative $\delta^{18}\text{O}$ values $< -15.0\text{‰}$ VPDB (Fig. 6a). The shift between the $\delta^{18}\text{O}$ value of the vein and the
419 $\delta^{18}\text{O}$ value of the surrounding host rock (Fig. 6d) increases from the western part of the belt (down to
420 -15.0‰ VPDB in Monte Corona and Monte Subasio) to the central and eastern part of the belt (up to
421 $+5.0\text{‰}$ VPDB in Monte Nero, Monte San Vicino, Monte Conero).

422 d. $^{87}\text{Sr}/^{86}\text{Sr}$ measurements

423 Analyses were carried out on 7 veins and 6 corresponding host rocks, distributed over three
424 structures of the UMAR (Monte Subasio, Monte Nero and Monte San Vicino, from the hinterland to
425 the foreland) and three formations (the Calcare Massiccio, the Maiolica, and the Scaglia Fms., Fig. 7,
426 Table 2). Vein sets sampled are the J1, J2 and J3 sets described in the whole area. $^{87}\text{Sr}/^{86}\text{Sr}$ values of
427 host rocks differ according to the formations, being the highest in the Scaglia Rossa Fm. ($^{87}\text{Sr}/^{86}\text{Sr} \approx$
428 0.70780), intermediate in the Calcare Massiccio Fm. ($^{87}\text{Sr}/^{86}\text{Sr} \approx 0.70760$), and the lowest in both the
429 Scaglia Bianca and the Maiolica Fm. ($^{87}\text{Sr}/^{86}\text{Sr} \approx 0.70730$). $^{87}\text{Sr}/^{86}\text{Sr}$ values of host rocks are in line with
430 expected values for seawater at the time of their respective deposition (McArthur et al., 2001).
431 $^{87}\text{Sr}/^{86}\text{Sr}$ values of veins scatter from 0.70740 to 0.70770, with lower values in the Monte Nero and in
432 the Monte San Vicino (0.707415 to 0.707646, irrespective of fracture set), and higher values in the
433 Monte Subasio (0.707644 to 0.707690, Set J2). One vein cement of J3 in the Monte Subasio returned
434 a lower $^{87}\text{Sr}/^{86}\text{Sr}$ value of 0.707437.

435 e. Carbonate clumped isotope paleothermometry ($\Delta_{47}\text{CO}_2$)

436 Sixteen samples were analyzed, including cements of NE-SW (J1) and NW-SE (J2) pre-folding
437 vein sets, along with coatings of early folding reverse (F1) and late folding strike-slip conjugate
438 mesoscale faults (F2). Regardless of the structural position in the individual folds, $\Delta_{47}\text{CO}_2$ values for
439 veins (Table 3) range from 0.511 ± 0.004 to 0.608 ± 0.000 ‰CDES in the Monte Corona (n=3), from 0.468
440 ± 0.032 to 0.574 ± 0.000 ‰CDES in the Monte Subasio (n=5), from 0.662 ± 0.004 to 0.685 ± 0.052 ‰CDES
441 in the Monte Nero (n=2), from 0.568 ± 0.035 to 0.658 ± 0.018 ‰CDES in the Monte San Vicino and the
442 syncline to its west (n=4), from 0.601 ± 0.032 to 0.637 ± 0.013 ‰CDES in the Monte Catria (n=2) and is
443 of 0.643 ± 0.044 ‰CDES in the Monte Conero. Corresponding $\delta^{18}\text{O}$ and $\delta^{13}\text{C}$ are reported in Table 2.
444 Analysis of $\Delta_{47}\text{CO}_2$ returns the precipitation temperature (T) and the oxygen isotopic values of the
445 mineralizing fluid can be calculated using the $\delta^{18}\text{O}$ of the mineral, the clumped isotope temperature
446 and the fractionation equation providing the fractionation coefficient α as a function of the
447 temperature T: $1000 \ln(\alpha) = 18.030 \times \frac{10^3}{T} - 32.420$ (Kim and O'Neil, 1997) (Fig. 8). Veins and faults
448 belong to the Calcare Massiccio Fm., the Maiolica Fm., the Scaglia Fm., and the marls of the Langhian
449 (Table 3). In the outermost structure studied (Monte Corona), the fractures of set J2 (n=2) yield
450 consistent precipitation temperatures $T = 106 \pm 8^\circ\text{C}$ and $\delta^{18}\text{O}_{\text{fluids}} = 0.0 \pm 1.8$ ‰ VSMOW; the sample of
451 the set J1 yields a $T = 56 \pm 16^\circ\text{C}$ and $\delta^{18}\text{O}_{\text{fluids}} = -1.1 \pm 1.8$ ‰ VSMOW; in the UMAR, at the Subasio
452 anticline, set F1 (n=3) returns temperatures T ranging from $80 \pm 5^\circ\text{C}$ to $141 \pm 19^\circ\text{C}$ and a corresponding
453 $\delta^{18}\text{O}_{\text{fluids}}$ ranging from 8.4 ± 1.0 ‰ to 16.1 ± 2.1 ‰ VSMOW, while the set J2 yields a $T = 71 \pm 0^\circ\text{C}$ and
454 $\delta^{18}\text{O}_{\text{fluids}} = -5.2 \pm 0.0$ ‰ VSMOW; in the Monte Nero, set J1 (n=2) yields consistent $T = 30 \pm 15^\circ\text{C}$ and
455 $\delta^{18}\text{O}_{\text{fluids}} = [2.7 \pm 2.4 \text{ to } 6.8 \pm 0.2]$ ‰ VSMOW; in the syncline on the west of the Monte San Vicino, set F2
456 (n=2) return $T = 36 \pm 4$ to $70 \pm 7^\circ\text{C}$ and $\delta^{18}\text{O}_{\text{fluids}} = 2.5 \pm 0.7$ to 8.3 ± 1.2 ‰ VSMOW; in the Monte San Vicino,
457 set J1 yields a $T = 47 \pm 5^\circ\text{C}$ and $\delta^{18}\text{O}_{\text{fluids}} = 3 \pm 1.1$ ‰ VSMOW while set J2 yields a $T = 74 \pm 10^\circ\text{C}$ and $\delta^{18}\text{O}_{\text{fluids}}$
458 $= 7.2 \pm 1.6$ ‰ VSMOW. In the Monte Catria, the sample of set J1 was characterized by a fluid with
459 $\delta^{18}\text{O}_{\text{fluids}} = 8.6 \pm 0.7$ ‰ VSMOW precipitated at $T = 44 \pm 4^\circ\text{C}$, the sample of set J2 by a fluid with $\delta^{18}\text{O}_{\text{fluids}} =$
460 11.1 ± 2.3 ‰ VSMOW precipitated at $T = 59 \pm 10^\circ\text{C}$. In the easternmost structure (Monte Conero), the
461 sample of J1 was characterized by a fluid with $\delta^{18}\text{O}_{\text{fluids}} = 5.8 \pm 2.4$ ‰ VSMOW precipitated at $T = 42$
462 $\pm 12^\circ\text{C}$.

463 f. U-Pb absolute dating of veins and faults

464 All samples from veins, whatever the set they belong to, reveal to have a U/Pb ratio not high
465 enough to return an age, with a too low U content and/or dominated by common lead (see
466 Supplementary material), which seems to be common in tectonic veins (Roberts et al., 2020). Of the
467 35 samples screened, 2 faults showed favorable $^{238}\text{U}/^{206}\text{Pb}$ ratios to allow for U-Pb dating (FAB5 and
468 FAB6) by applying the mapping approach. In sample FAB5, the pixels with higher U/Pb ratios made it
469 possible to obtain identical ages within the limits of uncertainty for the different plots in spite of a
470 majority of pixel values dominated by common lead (5.03 ± 1.2 Ma, 4.92 ± 1.3 Ma and 5.28 ± 0.95 Ma
471 for the TW, the 86TW and the isochron plot, respectively) (Fig 9a). The rather large age uncertainties
472 are consistent with the moderately high RSE values, but the d-MSWD values close to 1 indicate good
473 alignment of discretized data (Fig. 9b). In sample FAB6, the mapping approach returned distinct ages
474 according to the plot considered because of low U/Pb ratios (from 2.17 ± 1.4 Ma to 6.53 ± 2 Ma).
475 Keeping in mind their low reliability, the ages obtained for this sample grossly point toward
476 precipitation younger than ~ 8 Ma.

477

478 4. Interpretation

479 a. Sequence of fracturing events and related regional compressional and extensional 480 trends

481 The previously defined joint/vein, fault and stylolite sets were compared and gathered in order to
482 reconstruct the deformation history at the scale of the belt. We interpret the mesostructural network
483 as resulting from three stages of regional deformation, supported by already published fold-scale
484 fracture sequence ((Tavani and Cifelli, 2010; Tavani et al., 2008; Petracchini et al., 2012; Beaudoin et
485 al., 2016; Díaz General et al., 2015; Di Naccio et al., 2005; Vignaroli et al., 2013), and in line with the
486 ones observed in most recent studies (see Evans and Fischer, 2012; Tavani et al., 2015a for reviews) :
487 *Layer parallel shortening (LPS)* stage: chronological relationships statistically suggest that set J1
488 formed before set J2. Set J1 is kinematically consistent with set S1 that recorded bedding-parallel, NE-
489 SW directed Apenninic contraction, except in some places where sets J1 and S1 rather formed under
490 a slight local rotation/perturbations of the NE-SW directed compression as a result of structural
491 inheritance and/or of the arcuate shape of the fold. Bedding-parallel reverse faults of set F1 also
492 belong to this LPS stage as they are likely to develop at an early stage of fold growth (Tavani et al.,
493 2015).

494 *Folding* stage: set J2 reflects local extension perpendicular to fold axis and associated with strata
495 curvature at fold hinges. The extensional trend, i.e. the trend of J2 joints/veins, changes as a function
496 of curvature of fold axes in map view. We also interpret the stylolite peaks of which orientation are
497 intermediate between set S1 and S2 (Fig. 4) as related to the folding stage (Roure et al., 2005).

498 *Late stage fold tightening (LSFT)*: some tectonic stylolites with horizontal peaks striking NE-SW (set S2)
499 and some veins/joints (set J3) postdate strata tilting and are consistent with late folding strike-slip and
500 reverse faults (set F2). All these mesostructures formed slightly after the fold has locked, still under a
501 NE-SW contractional trend which is now oriented at a high angle to bedding. They mark a late stage
502 of fold tightening, when shortening is no longer accommodated by e.g., limb rotation.

503

504

505 b. Burial depth evolution and timing of contractional deformation

506 Stylolite roughness inversion applied to bedding-parallel stylolites (BPS) provides access to the
507 maximum depth experienced by the strata at the time vertical shortening was prevailing over
508 horizontal shortening (σ_1 vertical) (Ebner et al., 2009b; Koehn et al., 2007; Beaudoin et al., 2019;
509 Beaudoin et al., 2016; Beaudoin and Lacombe, 2018; Beaudoin et al., 2020; Rolland et al., 2014;
510 Bertotti et al., 2017). In this study, we will compare the depth range returned by the inversion of a
511 population of BPS to a local burial model (Fig. 10) reconstructed from the strata thickness documented
512 in wells located in the western-central part of the UMAR (Nero-Catria area) (Centamore et al., 1979;
513 Tavani et al., 2008). The resulting burial curves were constructed from the present-day strata
514 thicknesses corrected from (1) chemical compaction by increasing the thickness by an estimated 18%,
515 then from (2) physical compaction by using the opensource software *backstrip* (PetroMehas),
516 considering initial porosity of 70% for the carbonates and 40% for the sandstones, and compaction
517 coefficients of 0.58 and 0.30 derived from exponential decrease of porosity with increasing burial for
518 the carbonates and sandstones, respectively (Watts, 2001). The timing of exhumation was further
519 constrained by published paleogeothermometric studies and by the sedimentary record (Caricchi et
520 al., 2014; Mazzoli et al., 2002). To the west, tectonic reconstructions and organic matter
521 paleothermometry applied to the Tuscan Nappe (Caricchi et al., 2014) revealed that most of this unit
522 locally underwent more burial because it was underthrust below the Ligurian Nappe, but that the
523 western front of the Ligurian Nappe did not reach Monte Corona (Caricchi et al., 2014). We therefore
524 consider a unique burial curve for the whole western UMAR, and we project the range of depth values
525 at which individual BPS stopped being active on the burial curves of the formations hosting the BPS.
526 Recent application of this technique, coupled with absolute dating of vein cements (Beaudoin et al.,
527 2018), showed that the greatest depth that a population of BPS recorded was reached nearly at the
528 time corresponding to the age of the oldest LPS-related veins, suggesting that it is possible to constrain
529 the timing at which horizontal principal stress overcame the vertical principal stress, switching from
530 burial-related stress regime (σ_1 vertical) to LPS (σ_1 horizontal) (Beaudoin et al., 2020). In the case of
531 the UMAR, 800m is the minimum depth at which dissolution stopped along BPS planes, regardless of
532 studied formations. That confirms that burial-related pressure solution (*i.e.*, chemical vertical
533 compaction) likely initiated at depth shallower than 800 m (Ebner et al., 2009b; Rolland et al., 2014;
534 Beaudoin et al., 2019; Beaudoin et al., 2020).

535 Figure 10 also shows that BPS were active mainly from the Cretaceous (age of deposition of
536 the platform) until Langhian times (~15 Ma), which suggests that σ_1 likely switched from vertical to
537 horizontal at ca. 15 Ma. For the sake of simplicity, we will consider this age of 15 Ma for the onset of
538 LPS, but one must keep in mind that taking into account a 12% uncertainty on the magnitude of the
539 maximum vertical stress derived from stylolite roughness inversion, hence $\pm 12\%$ on the determined
540 depth, yields a 19 to 12 Ma possible time span for the onset of LPS (from Burdigalian to Serravalian)
541 (Fig. 10). Sedimentary record pins the beginning of folding of the UMAR to the Tortonian (11-7.3 Ma)
542 in the west and to the Messinian (7.3-5.3 Ma) in the east (onshore) (Calamita et al., 1994).
543 Consequently, in the central and western part of the UMAR, we propose that the LPS stage of
544 Apennine contraction lasted about ~7 Ma (from 15 to 8 Ma - Langhian to Tortonian-) before folding
545 occurred. Absolute dating of faults related to late stage fold tightening in the central part of the UMAR
546 further indicates that fold development was over by ~5 Ma, *i.e.* by the beginning of the Pliocene (5.3-
547 1.75 Ma). We can therefore estimate an average duration of folding in the western-central part of the
548 UMAR of ~3 Ma. Knowing the oldest record of post-orogenic extensional tectonics in the UMAR is mid-
549 Pliocene (~3 Ma) (Barchi, 2010), we can also estimate the duration of the LSFT to ~2 Ma. In total, the

550 probable period when the compressive horizontal principal stress σ_1 was higher in magnitude than
551 the vertical stress (*i.e.* until post-orogenic extension) lasted for 9 Ma in the Western-Central part of
552 the UMAR. We propose an average duration of fold growth about 3 Ma, quite in accordance with
553 previous attempts to constrain fold growth duration elsewhere using either syntectonic
554 sedimentation (3 to 10 Ma (Holl and Anastasio, 1993; Anastasio et al., 2018), up to 24 Ma with
555 quiescent periods in between growth pulses (Masaferro et al., 2002)); or mechanical or kinematic
556 modeling applied to natural cases (1 Ma to 8 Ma (Suppe et al., 1992; Yamato et al., 2011)). The
557 combination of bedding-parallel stylolite inversion, burial models and U-Pb dating of vein
558 cements/fault coatings yields a valuable insight into the timing of the different stages of contraction
559 in a fold-and-thrust belt (Beaudoin et al., 2018).

560 c. Paleofluid system evolution

561 The combined use of BPS inversion and burial curves constrains the absolute timing of LPS,
562 folding and LSFT in the UMAR (Fig. 10). The further combination of this calendar with the knowledge
563 of the past geothermal gradient as reconstructed from organic matter studies in the eastern part of
564 the TN (23°C/km, Caricchi et al., 2014) therefore yields the expected temperature within the various
565 strata at the time vein sets J1, J2 and J3 and faults F1 and F2 formed. Then it is possible to identify
566 whether fluids precipitated at thermal equilibrium or not during the Apenninic contraction. Overall,
567 most calcite grains from vein cements show thin twins (thickness < 5 μm) and rectilinear, suggesting
568 deformation at temperature below 170°C (Ferrill et al., 2004; Lacombe, 2010), in line with the
569 maximum expected temperature reached by the Upper Triassic – Eocene carbonate reservoir (120°C,
570 Fig. 10). The fact $\delta^{13}\text{C}$ values of veins are very close to the $\delta^{13}\text{C}$ values of the surrounding host rocks
571 (Fig. 6c) while the $\delta^{18}\text{O}$ values of the veins are different from the $\delta^{18}\text{O}$ values of the host (Fig. 6d)
572 discards that the fluids' original isotopic signatures were lost due to rock buffering. The similarity of
573 $\delta^{13}\text{C}$ values of veins compared to local host-rock, along with the $^{87}\text{Sr}/^{86}\text{Sr}$ values of the veins, that are
574 in accordance with the expected values of the host rocks (Fig. 7) (McArthur et al., 2001), points
575 towards very limited exchange between stratigraphic reservoirs and rules out external fluid input into
576 the system. Indeed, other potential fluid reservoirs such as lower Triassic evaporites seawater have
577 $^{87}\text{Sr}/^{86}\text{Sr}$ values significantly higher (0.70800-0.70820) than the highest $^{87}\text{Sr}/^{86}\text{Sr}$ values documented in
578 the UMAR (Monte Subasio, 0.70760-0.70770; Fig. 7). These characteristics indicate a closed fluid
579 system in most of the UMAR, with formational fluids precipitating at thermal equilibrium, limited
580 reservoir fluid - host rock interactions in the reservoirs and limited cross-strata fluid migrations.

581 When considering $\delta^{18}\text{O}$ and $\Delta_{47}\text{CO}_2$ values, the folds in the westernmost part of the UMAR,
582 Monte Corona and Monte Subasio, require a different interpretation from the other folds of the UMAR
583 (Fig. 6d). Indeed, if considering an environment with limited connection between reservoirs and no
584 implication of external fluids, *i.e.* where fluids are sourced locally from the marine carbonates, the fact
585 that in the western part of the UMAR, the $\delta^{18}\text{O}$ values of the veins are significantly more positive than
586 the $\delta^{18}\text{O}$ values of their host-rocks implies that fluids that precipitated were enriched in ^{18}O isotope
587 relative to the original formational fluid. Such a fractionation is usually interpreted as the result of
588 rock dissolution during fluid migration (Clayton et al., 1966; Hitchon and Friedman, 1969). This is
589 further supported by the $\delta^{18}\text{O}_{\text{fluids}}$ values derived from $\Delta_{47}\text{CO}_2$ measurements, that are higher in the
590 Monte Subasio (8 to 16‰ VSMOW, Fig. 8) than in the rest of the UMAR (from 0 to 8‰ VSMOW, Fig.
591 8), witnessing a higher degree of reservoir fluid-rock interaction in the western part of the UMAR.

592 Temperatures of precipitation are consistent with the predicted temperatures of host rocks
593 considering the formation and timing of fracture development in most of the UMAR at all times of
594 deformation (Figs. 6-7-10). This is different in Monte Corona and Monte Subasio where veins
595 precipitated from fluids at higher temperature than the predicted temperatures for the host-rock. In
596 the Maiolica Fm. at Monte Corona, J2 veins returned a temperature > 100°C while the maximum
597 predicted temperature during folding is < 90°C. In the Scaglia Fm. at Monte Subasio, the LPS-related
598 veins (J1) and faults (F1) precipitated from fluids much hotter (105 -140°) than the predicted
599 temperature during LPS (<70°C). The interpretation of an easternward migration of hydrothermal
600 basinal brines with high degree of fluid-rock interaction affecting the western part of the UMAR is
601 further supported by higher the ⁸⁷Sr/⁸⁶Sr ratios in Monte Subasio (Fig. 7). A hydrothermal dolomitizing
602 fluid migration event was documented in the southeastern part of the UMAR (Montagna dei Fiori),
603 and interpreted as vertical fluid migration from deeper Jurassic reservoirs (Mozafari et al., 2019; Storti
604 et al., 2018). But the reconstructed fluid temperatures (100°C) and δ¹⁸O_{fluids}(6‰ VSMOW) are still
605 much lower than the ones reconstructed from the fluids involved in the Monte Subasio (105-140°C; 9
606 to 15‰ VSMOW), supporting that a different fluid system was prevailing in the westernmost part of
607 the belt during LPS, folding and LSFT compared to central-eastern UMAR.

608 5. Discussion

609 a. Fluid origin and engine of migration in the westernmost Umbria-Marches Apennine 610 Ridge

611 During LPS and folding, a temperature of fluid precipitation of up to 140°C, i.e., significantly
612 higher than the local host-rock temperature, implies that fluids flowed from depth >4 km, while a high
613 δ¹⁸O_{fluids} reflects a high degree of reservoir fluid-rock interaction. Considering the subsurface geometry
614 of the UMAR (Fig. 1) and discarding any input of external fluids originated from the lower Triassic
615 formations or from the basement on the basis of ⁸⁷Sr/⁸⁶Sr values, we propose that the fluids originated
616 from the westward lateral extension of the carbonate platform reservoir that was buried under the
617 Tuscan Nappe and Ligurian Nappe (Caricchi et al., 2014; Carboni et al., 2020). The coexistence inside
618 a single deformation stage (LPS or folding) of both local/meteoritic fluids and hydrothermal brines that
619 migrated from depths can be explained by transient flushes into the system of hydrothermal fluids
620 flowing from deeply buried parts of the same, stratigraphically continuous, reservoir (Bachu, 1995;
621 Garven, 1995; Machel and Cavell, 1999; Oliver, 1986).

622 We therefore propose that the fluid system prevailing at the Monte Corona and at the Monte
623 Subasio reflects an eastward, squeegee-type, flow of hydrothermal fluids (Fig. 11). The long-term
624 migration engine is the lateral variation of the burial depth of the reservoir related to the stacked
625 Tuscan and Ligurian Nappes in the west of the UMAR (up to 4 km for the Scaglia Fm., Caricchi et al.,
626 2014), that does not affect the UMAR (burial up to 3 km for the Scaglia Fm., Figs. 10, 11b). This depth
627 variation likely created a difference in hydraulic head, and so a hydraulic gradient allowing for the
628 eastward fluid migration within the reservoir, enhanced by LPS and related fracture development
629 (Roure et al., 2005). As the paleodepth variation was related to the thickness of the nappes stacking
630 rather than to a foreland-type slope, the UMAR would then have formed a kind of 'plateau' without
631 any large-scale lateral fluid migration (Fig. 11b). The inferred pulses of hydrothermal fluids also imply
632 a strong influence of foreland-ward propagation of contractional deformation on the eastward fluid
633 expellation (Oliver, 1986; Machel and Cavell, 1999).

634

635

b. Influence of tectonic style on fluid flow during deformation history

636

637

638

639

640

641

642

643

The study of the calcite cements that precipitated in tectonically controlled veins and faults at the scale of the UMAR and TN distinguishes two different fluid flow histories. East of Monte Subasio, *i.e.*, in the UMAR where shortening is distributed on deep-rooted faults, geochemical data reveal a closed fluid system, with formational fluids precipitating at thermal equilibrium, limited fluid - host rock interactions in the reservoirs and limited cross-strata fluid migration. In contrast, on the western part of this divide (in the TN), where shortening was accommodated by stacked nappes detached above the Triassic décollement level, high temperatures of fluids suggest the occurrence of eastward large-scale pulses of hydrothermal fluids (squeegee type, Fig. 11b).

644

645

646

647

648

649

650

651

652

653

654

655

656

657

658

659

660

661

662

663

664

665

666

667

668

If considering a thin-skinned tectonic model for the UMAR with shallow, low angle thrusts rooting into the Triassic evaporitic décollement (Fig. 1) (Bally et al., 1986), one would expect some influence of Triassic fluids signatures to be involved in the reservoir paleohydrology at the time faults were active or during folding, as illustrated in similar salt-detached fold systems in the Pyrenees, in the Appalachians, and in the Sierra Madre Oriental (Lacroix et al., 2011; Travé et al., 2000; Evans and Hobbs, 2003; Evans and Fischer, 2012; Fischer et al., 2009; Smith et al., 2012; Lefticariu et al., 2005). On the other hand, if considering a thick-skinned tectonic model with high angle thrusts crossing the Triassic down to the basement, it becomes more likely that these thrusts did not act as efficient conduits for deep fluids (evaporitic fluids or basement fluids) as fault damage zones in evaporites remains non permeable, if the displacement along the faults is smaller than the non-permeable layer thickness. This contrasts with paleohydrological studies of basement cored folds, where high angle thrusts allow hot flashes of hydrothermal fluids into the overlying cover (Beaudoin et al., 2011; Evans and Fischer, 2012) in the absence of evaporites. Thus, the lack of Triassic influence in our paleofluid dataset seems to support a thick-skinned tectonic style of deformation in the UMAR (Fig. 11c). This fluid flow model therefore outlines important differences between belts where shortening is localized and accommodated by shallow nappe stacking, typical from thin-skinned belts, and belts where shortening is instead distributed on basement-cored folds related to high angle thrusts, typical of thick-skinned belts (Lacombe and Bellahsen, 2016). Squeegee-type fluid flow during LPS in response to hydraulic gradient and lateral tectonic contraction has also been described in other thin-skinned belts, such as the Canadian Rocky Mountains (Vandeginste et al., 2012; Roure et al., 2010; Machel and Cavell, 1999; Qing and Mountjoy, 1992), or in Venezuela (Schneider et al., 2002; Schneider et al., 2004; Roure et al., 2003) where lithospheric bulging was at the origin of the depth difference leading to hydraulic gradient-driven fluid migration. The presented case study shows how stacking of sedimentary units typical of thin-skinned tectonics strongly influences the fluid system beyond the morphological front of the belt and allows occurrence of large-scale fluid migration.

669

6. Conclusions

670

671

672

673

674

675

676

Our study of the vein-fault-tectonic stylolite populations distributed in Jurassic to Eocene limestone rocks at the scale of the thin-skinned Tuscan Nappe and presumably thick-skinned Umbria-Marche Apennine Ridge reveals the occurrence of several fracture/stylolite sets that support a three stage (meso)structural evolution of the Apenninic contraction: (1) layer-parallel shortening is reconstructed by a set of joint/veins striking NE-SW to E-W, perpendicular to the local trend of the fold, alongside with stylolite peaks striking NE-SW, and early folding bedding-parallel reverse faults; (2) the folding stage is recorded by fold-parallel mode I joints and veins; (3) the late stage fold

677 tightening is recorded by post-tilting, late folding stylolite peaks, joints/veins and also mesoscale
678 reverse and strike-slip faults.

679 Thanks to burial models coupled to bedding-parallel stylolite paleopiezometry, along with
680 (unfortunately scarce) U-Pb absolute dating of strike-slip faults related to late stage fold tightening,
681 we were able to reconstruct the timing of the onset and the duration of the Apennine contraction:
682 the LPS likely started by Langhian time (*ca.* 15 Ma, inferred from the bedding-parallel stylolite
683 inversion combined to burial model), lasted for *ca.* 7 Ma, then folding started by the Tortonian time
684 (*ca.* 8 Ma, as constrained by the sedimentary record of growth strata), lasted for *ca.* 3 Ma, LFST started
685 by the beginning of Pliocene (*ca.* 5 Ma, given by absolute dating of fault coatings), itself lasting for 2
686 Ma before post-orogenic extension affected strata since mid-Pliocene (3 Ma).

687 Accessing the starting and ending time of deformation in the UMAR also allowed us to predict the
688 depth and expected temperatures of the paleofluid during fracturing assuming fluids precipitated at
689 thermal equilibrium. By characterizing the cements related to sets of veins and faults using $\delta^{18}\text{O}$ and
690 $\delta^{13}\text{C}$, $^{87}/^{86}\text{Sr}$, and $\Delta_{47}\text{CO}_2$ values, we show that different paleofluid systems occurred during LPS and
691 folding from west to east of the section. In the westernmost folds of the UMAR located beyond the
692 arrow of the Ligurian Nappe thrusting over the Tuscan Nappe, we highlight a local fluid system with
693 transient large-scale lateral, stratigraphically compartmentalized hydrothermal fluid migration. In
694 contrast, these pulses are not documented in the rest of the UMAR and its foreland, where the fluid
695 system remained closed at all time. We tentatively relate this change in fluid system to a lateral change
696 in tectonic style of deformation across the belt, from thin-skinned in the TN to rather thick-skinned in
697 the UMAR. Beyond regional implications, the promising combination of stylolite roughness inversion
698 and burial history reconstruction, linked to reliable past geothermal gradient appears as a powerful
699 tool to unravel coupled structural and fluid flow evolution in fold-and-thrust belts.

700 Author contribution

701 NB, OL, DK, A. Billi, JPC were involved in the overall writing of the manuscript led by NB; NB, OL, DK,
702 A. Billi collected structural data and rock samples in the field; NB, AL and OL conducted microstructural
703 inversion; GH, A. Boyce, CJ, MM, NR, IM, FC and CP designed experiments and collected the
704 geochemical data and wrote the related parts of the manuscript and appendices. All authors critically
705 reviewed the multiple drafts of the manuscript.

706

707 7. Acknowledgments

708 This work has received funding from the Natural Environmental Research Council under grant number
709 IP-1494-1114, from European Union's Seventh Framework Program for research, technological
710 development, and demonstration under grant agreement 316889, and it also received funds from
711 Sorbonne Université (research agreement C14313). NB is funded through the ISITE program E2S,
712 supported by ANR PIA and Région Nouvelle-Aquitaine. Authors also thank two anonymous reviewers
713 for insightful comments that improved the manuscript, and Randolph Williams for his editorial work.

714 References

715

716 Agosta, F., Alessandrini, M., Antonellini, M., Tondi, E., and Giorgioni, M.: From fractures to flow: A
717 field-based quantitative analysis of an outcropping carbonate reservoir, *Tectonophysics*, 490, 197-
718 213, 10.1016/j.tecto.2010.05.005, 2010.

719 Agosta, F., Luetkemeyer, P. B., Lamarche, J., Crider, J. G., and Lacombe, O.: An introduction to the
720 Special Issue: The role of fluids in faulting and fracturing in carbonates and other upper crustal rocks,
721 *Tectonophysics*, 690, 1-3, 2016.

722 Ahmadhadi, F., Daniel, J. M., Azzizadeh, M., and Lacombe, O.: Evidence for pre-folding vein
723 development in the Oligo-Miocene Asmari Formation in the Central Zagros Fold Belt, Iran, *Tectonics*,
724 27, 2008.

725 Amrouch, K., Lacombe, O., Bellahsen, N., Daniel, J. M., and Callot, J. P.: Stress and strain patterns,
726 kinematics and deformation mechanisms in a basement-cored anticline: Sheep Mountain Anticline,
727 Wyoming, *Tectonics*, 29(1), TC1005, 2010

728 Anastasio, D., Kodama, K., and Parés, J.: Episodic deformation rates recovered from growth strata,
729 Pyrenees, *Search and Discovery Article*, 30553, 2018.

730 Andresen, K. J.: Fluid flow features in hydrocarbon plumbing systems: What do they tell us about the
731 basin evolution?, *Marine Geology*, 332, 89-108, 2012.

732 Angelier, J.: Tectonic analysis of fault slip data sets, *Journal of Geophysical Research: Solid Earth*, 89,
733 5835-5848, 1984.

734 Bachu, S.: Synthesis and model of formation-water flow, Alberta Basin, Canada, *AAPG Bulletin*, 79,
735 1159-1178, 1995.

736 Bally, A., Burbi, L., Cooper, C., and Ghelardoni, R.: Balanced cross sections and seismic reflection
737 profiles across the central Apennines Mem, *Soc. Geol. It.*, 35, 275-310, 1986.

738 Barbier, M., Hamon, Y., Callot, J.-P., Floquet, M., and Daniel, J.-M.: Sedimentary and diagenetic
739 controls on the multiscale fracturing pattern of a carbonate reservoir: The Madison Formation (Sheep
740 Mountain, Wyoming, USA), *Marine and Petroleum Geology*, 29, 50-67,
741 10.1016/j.marpetgeo.2011.08.009, 2012.

742 Barchi, M., De Feyter, A., Magnani, M., Minelli, G., Piali, G., and Sotera, B.: Extensional tectonics in
743 the Northern Apennines (Italy): evidence from the CROP03 deep seismic reflection line, *Mem. Soc.*
744 *Geol. It.*, 52, 527-538, 1998.

745 Barchi, M.: The Neogene–Quaternary evolution of the Northern Apennines: crustal structure, style of
746 deformation and seismicity, *Journal of Virtual Explorer*, 36, 2010.

747 Beaudoin, N., Bellahsen, N., Lacombe, O., and Emmanuel, L.: Fracture-controlled paleohydrogeology
748 in a basement-cored, fault-related fold: Sheep Mountain Anticline, Wyoming, United States,
749 *Geochemistry, Geophysics, Geosystems*, 12, Q06011, 10.1029/2010gc003494, 2011.

750 Beaudoin, N., Leprêtre, R., Bellahsen, N., Lacombe, O., Amrouch, K., Callot, J.-P., Emmanuel, L., and
751 Daniel, J.-M.: Structural and microstructural evolution of the Rattlesnake Mountain Anticline
752 (Wyoming, USA): new insights into the Sevier and Laramide orogenic stress build-up in the Bighorn
753 Basin, *Tectonophysics*, 576, 20-45, 2012.

754 Beaudoin, N., Lacombe, O., Bellahsen, N., and Emmanuel, L.: Contribution of studies of sub-seismic
755 fracture populations to paleo-hydrological reconstructions (Bighorn Basin, USA), *Procedia Earth and*
756 *Planetary Science*, 7, 57-60, 2013.

757 Beaudoin, N., Bellahsen, N., Lacombe, O., Emmanuel, L., and Pironon, J.: Crustal-scale fluid flow during
758 the tectonic evolution of the Bighorn Basin (Wyoming, USA), *Basin Research*, 26, 403-435,
759 10.1111/bre.12032, 2014.

760 Beaudoin, N., Koehn, D., Lacombe, O., Lecouty, A., Billi, A., Aharonov, E., and Parlangeau, C.:
761 Fingerprinting stress: Stylolite and calcite twinning paleopiezometry revealing the complexity of
762 progressive stress patterns during folding-The case of the Monte Nero anticline in the Apennines, Italy,
763 *Tectonics*, 35, 1687-1712, 10.1002/2016tc004128, 2016.

764 Beaudoin, N., and Lacombe, O.: Recent and future trends in paleopiezometry in the diagenetic
765 domain: Insights into the tectonic paleostress and burial depth history of fold-and-thrust belts and
766 sedimentary basins, *Journal of Structural Geology*, 114, 357-365, 10.1016/j.jsg.2018.04.001, 2018.

767 Beaudoin, N., Lacombe, O., Roberts, N. M. W., and Koehn, D.: U-Pb dating of calcite veins reveals
768 complex stress evolution and thrust sequence in the Bighorn Basin, Wyoming, USA, *Geology*, 46, 1015-
769 1018, 10.1130/g45379.1, 2018.

770 Beaudoin, N., Gasparrini, M., David, M.-E., Lacombe, O., and Koehn, D.: Bedding-parallel stylolites as
771 a tool to unravel maximum burial depth in sedimentary basins: Application to Middle Jurassic
772 carbonate reservoirs in the Paris basin, France, *GSA Bulletin*, 131, 1239-1254, 10.1130/b32064.1,
773 2019.

774 Beaudoin N., Huyghe D., Bellahsen N., Lacombe O., Emmanuel L., Mouthereau F., and Ouahnon L.:
775 Fluid systems and fracture development during syn-depositional fold growth : example from the Pico
776 del Aguila Anticline, Sierras Exteriores, Southern Pyrenees, Spain. *Journal of Structural Geology*, 70,
777 23-38, 2015

778 Beaudoin, N., Lacombe, O., Koehn, D., David, M.-E., Farrell, N., and Healy, D.: Vertical stress history
779 and paleoburial in foreland basins unravelled by stylolite roughness paleopiezometry: Insights from
780 bedding-parallel stylolites in the Bighorn Basin, Wyoming, USA, *Journal of Structural Geology*, 104061,
781 10.1016/j.jsg.2020.104061, 2020.

782 Becker, S., Eichhubl, P., Laubach, S. E., Reed, R. M., Lander, R., and Bodnar, R.: A 48 my history of
783 fracture opening, temperature, and fluid pressure: Cretaceous Travis Peak Formation, East Texas
784 basin, *Bulletin*, 122, 1081-1093, 2010.

785 Bellahsen, N., Fiore, P., and Pollard, D. D.: The role of fractures in the structural interpretation of Sheep
786 Mountain Anticline, Wyoming, *Journal of Structural Geology*, 28, 850-867, 2006.

787 Bergbauer, S., and Pollard, D. D.: A new conceptual fold-fracture model including prefolding joints,
788 based on the Emigrant Gap anticline, Wyoming, *Geological Society of America Bulletin*, 116, 294-307,
789 2004.

790 Bernasconi, S. M., Hu, B., Wacker, U., Fiebig, J., Breitenbach, S. F., and Rutz, T.: Background effects on
791 Faraday collectors in gas-source mass spectrometry and implications for clumped isotope
792 measurements, *Rapid Communications in Mass Spectrometry*, 27, 603-612, 2013.

793 Bertotti, G., de Graaf, S., Bisdorn, K., Oskam, B., B. Vonhof, H., H. R. Bezerra, F., J. G. Reijmer, J., and L.
794 Cazarin, C.: Fracturing and fluid-flow during post-rift subsidence in carbonates of the Jandaíra
795 Formation, Potiguar Basin, NE Brazil, *Basin Research*, 29, 836-853, 10.1111/bre.12246, 2017.

796 Bjørlykke, K.: Fluid flow in sedimentary basins, *Sedimentary Geology*, 86, 137-158, 1993.

797 Bjørlykke, K.: Fluid-flow processes and diagenesis in sedimentary basins, *Geological Society, London,*
798 *Special Publications*, 78, 127-140, 1994.

799 Bjørlykke, K.: Subsurface Water and Fluid Flow in Sedimentary Basins, in: *Petroleum Geoscience*, 259-
800 279, 2010.

801 Butler, R. W. H., Mazzoli, S., Corrado, S., Donatis, M. D., Bucci, D. D., Gambini, R., Naso, G., Nicolai, C.,
802 Scrocca, D., Shiner, P., and Zucconi, V.: Applying Thick-skinned Tectonic Models to the Apennine Thrust
803 Belt of Italy—Limitations and Implications. 2004.

804 Calamita, F., and Deiana, G.: The arcuate shape of the Umbria-Marche-Sabina Apennines (central
805 Italy), *Tectonophysics*, 146, 139-147, 1988.

806 Calamita, F., Cello, G., Deiana, G., and Paltrinieri, W.: Structural styles, chronology rates of
807 deformation, and time-space relationships in the Umbria-Marche thrust system (central Apennines,
808 Italy), *Tectonics*, 13, 873-881, 1994.

809 Callot, J.-P., Breesch, L., Guilhaumou, N., Roure, F., Swennen, R., and Vilasi, N.: Paleo-fluids
810 characterisation and fluid flow modelling along a regional transect in Northern United Arab Emirates
811 (UAE), *Arabian Journal of Geosciences*, 3, 413-437, 2010.

812 Callot, J.-P., Roure, F., Faure, J.-L., and Tarapoanca, M.: Kinematic, thermal, and petroleum modeling
813 of the northern Emirates, in: *Petroleum System Analysis - Case Studies: AAPG Memoir*, edited by:
814 AbuAli, M. A., Moretti, I., and Nordgård Bolås, H. M., 135-164, 2017a.

815 Callot, J.-P., Sassi, W., Roure, F., Hill, K., Wilson, N., and Divies, R.: Pressure and Basin Modeling in
816 Foothill Belts: A Study of the Kutubu Area, Papua New Guinea Fold and Thrust Belt, in: *Petroleum*

817 Systems Analysis: AAPG Memoir, edited by: AbuAli, M. A., Moretti, I., and Nordgård Bolås, H. M., 165-
818 190, 2017b.

819 Carboni, F., Brozzetti, F., Mirabella, F., Cruciani, F., Porreca, M., Ercoli, M., Back, S., and Barchi, M. R.:
820 Geological and geophysical study of a thin-skinned tectonic wedge formed during an early collisional
821 stage: the Trasimeno Tectonic Wedge (Northern Apennines, Italy), *Geological Magazine*, 157, 213-232,
822 2020.

823 Caricchi, C., Aldega, L., and Corrado, S.: Reconstruction of maximum burial along the Northern
824 Apennines thrust wedge (Italy) by indicators of thermal exposure and modeling, *Geological Society of
825 America Bulletin*, 127, 428-442, 10.1130/b30947.1, 2014.

826 Caricchi, C., Aldega, L., and Corrado, S.: Reconstruction of maximum burial along the Northern
827 Apennines thrust wedge (Italy) by indicators of thermal exposure and modeling, *Bulletin*, 127, 428-
828 442, 2015.

829 Carminati, E., Lustrino, M., Cuffaro, M., and Doglioni, C.: Tectonics, magmatism and geodynamics of
830 Italy: What we know and what we imagine, *Journal of the Virtual Explorer*, 36,
831 10.3809/jvirtex.2010.00226, 2010.

832 Cartwright, J.: The impact of 3D seismic data on the understanding of compaction, fluid flow and
833 diagenesis in sedimentary basins, *Journal of the Geological Society*, 164, 881-893, 2007.

834 Cello, G., Mazzoli, S., Tondi, E., and Turco, E.: Active tectonics in the central Apennines and possible
835 implications for seismic hazard analysis in peninsular Italy, *Tectonophysics*, 272, 43-68, 1997.

836 Centamore, E., Chiocchini, M., Chiocchini, U., Dramis, F., Giardini, G., Jacobacci, A., Martelli, G.,
837 Micarelli, A., and Potetti, M.: Carta Geologica d'Italia alla scala 1: 50.000. Note Illustrative F° 301
838 «Fabriano», 1979.

839 Clayton, R., Friedman, I., Graf, D., Mayeda, T., Meents, W., and Shimp, N.: The origin of saline
840 formation waters: 1. Isotopic composition, *Journal of Geophysical Research*, 71, 3869-3882, 1966.

841 Conti, S., and Gelmini, R.: Miocene-Pliocene tectonic phases and migration of foredeep-thrust belt
842 system in Northern Apennines, *J Mem. Soc. Geol. It*, 48, 261-274, 1994.

843 Cruset, D., Cantarero, I., Travé, A., Vergés, J., and John, C. M.: Crestal graben fluid evolution during
844 growth of the Puig-reig anticline (South Pyrenean fold and thrust belt), *Journal of Geodynamics*, 101,
845 30-50, 2016.

846 Cruset, D., Cantarero, I., Vergés, J., John, C. M., Muñoz-López, D., and Travé, A.: Changes in fluid regime
847 in syn-orogenic sediments during the growth of the south Pyrenean fold and thrust belt, *Global and
848 Planetary Change*, 171, 207-224, 10.1016/j.gloplacha.2017.11.001, 2018.

849 d'Agostino, N., Jackson, J., Dramis, F., and Funiciello, R.: Interactions between mantle upwelling,
850 drainage evolution and active normal faulting: an example from the central Apennines (Italy),
851 *Geophysical Journal International*, 147, 475-497, 2001.

852 Dale, A., John, C. M., Mozley, P. S., Smalley, P., and Muggeridge, A. H.: Time-capsule concretions:
853 unlocking burial diagenetic processes in the Mancos Shale using carbonate clumped isotopes, *Earth
854 and Planetary Science Letters*, 394, 30-37, 2014.

855 Davies, A. J., and John, C. M.: The clumped ($^{13}\text{C}^{18}\text{O}$) isotope composition of echinoid calcite: Further
856 evidence for "vital effects" in the clumped isotope proxy, *Geochimica et Cosmochimica Acta*, 245, 172-
857 189, 2019.

858 De Graaf, S., Nooitgedacht, C. W., Le Goff, J., Van Der Lubbe, J. H., Vonhof, H. B., and Reijmer, J. J.:
859 Fluid-flow evolution in the Albanide fold-thrust belt: Insights from hydrogen and oxygen isotope ratios
860 of fluid inclusions, *AAPG Bulletin*, 103, 2421-2445, 2019.

861 Defliese, W. F., Hren, M. T., and Lohmann, K. C.: Compositional and temperature effects of phosphoric
862 acid fractionation on $\Delta 47$ analysis and implications for discrepant calibrations, *Chemical Geology*, 396,
863 51-60, 2015.

864 Dennis, K. J., Affek, H. P., Passey, B. H., Schrag, D. P., and Eiler, J. M.: Defining an absolute reference
865 frame for 'clumped' isotope studies of CO_2 , *Geochimica Cosmochimica Acta*, 75, 7117-7131, 2011.

866 Di Naccio, D., Boncio, P., Cirilli, S., Casaglia, F., Morettini, E., Lavecchia, G., and Brozzetti, F.: Role of
867 mechanical stratigraphy on fracture development in carbonate reservoirs: Insights from outcropping

868 shallow water carbonates in the Umbria–Marche Apennines, Italy, *Journal of Volcanology and*
869 *Geothermal Research*, 148, 98-115, 10.1016/j.jvolgeores.2005.03.016, 2005.

870 Díaz General, E. N., Mollema, P. N., and Antonellini, M.: Fracture patterns and fault development in
871 the pelagic limestones of the Monte Conero Anticline (Italy), *Italian Journal of Geosciences*, 134, 495-
872 512, 2015.

873 Donard, A., Pottin, A.-C., Pointurier, F., and Pécheyran, C.: Determination of relative rare earth
874 element distributions in very small quantities of uranium ore concentrates using femtosecond UV laser
875 ablation–SF-ICP-MS coupling, *Journal of Analytical Atomic Spectrometry*, 30, 2420-2428, 2015.

876 Ebner, M., Koehn, D., Toussaint, R., and Renard, F.: The influence of rock heterogeneity on the scaling
877 properties of simulated and natural stylolites, *Journal of Structural Geology*, 31, 72-82,
878 10.1016/j.jsg.2008.10.004, 2009a.

879 Ebner, M., Koehn, D., Toussaint, R., Renard, F., and Schmittbuhl, J.: Stress sensitivity of stylolite
880 morphology, *Earth and Planetary Science Letters*, 277, 394-398, 10.1016/j.epsl.2008.11.001, 2009b.

881 Ebner, M., Piazzolo, S., Renard, F., and Koehn, D.: Stylolite interfaces and surrounding matrix material:
882 Nature and role of heterogeneities in roughness and microstructural development, *Journal of*
883 *Structural Geology*, 32, 1070-1084, 10.1016/j.jsg.2010.06.014, 2010.

884 Elter, F. M., Elter, P., Eva, C., Eva, E., Kraus, R. K., Padovano, M., and Solarino, S.: An alternative model
885 for the recent evolution of the Northern–Central Apennines (Italy), *Journal of Geodynamics*, 54, 55-
886 63, 2012.

887 Engelder, T.: The role of pore water circulation during the deformation of foreland fold and thrust
888 belts, *Journal of Geophysical Research: Solid Earth*, 89, 4319-4325, 1984.

889 Evans, M., and Hobbs, G.: Fate of ‘warm’ migrating fluids in the central Appalachians during the Late
890 Paleozoic Alleghanian orogeny, *Journal of Geochemical Exploration*, 78, 327-331, 2003.

891 Evans, M. A., Tollo, R., Bartholomew, M., Hibbard, J., and Karabinos, P.: Temporal and spatial changes
892 in deformation conditions during the formation of the Central Appalachian fold-and-thrust belt:
893 Evidence from joints, vein mineral paragenesis, and fluid inclusions, *From Rodinia to Pangea: The*
894 *Lithotectonic Record of the Appalachian Region*, 206, 477, 2010.

895 Evans, M. A., and Fischer, M. P.: On the distribution of fluids in folds: A review of controlling factors
896 and processes, *Journal of Structural Geology*, 44, 2-24, 2012.

897 Ferrill, D. A., Morris, A. P., Evans, M. A., Burkhard, M., Groshong Jr, R. H., and Onasch, C. M.: Calcite
898 twin morphology: a low-temperature deformation geothermometer, *Journal of structural Geology*,
899 26, 1521-1529, 2004.

900 Fischer, M. P., Higuera-Díaz, I. C., Evans, M. A., Perry, E. C., and Lefticariu, L.: Fracture-controlled
901 paleohydrology in a map-scale detachment fold: Insights from the analysis of fluid inclusions in calcite
902 and quartz veins, *Journal of Structural Geology*, 31, 1490-1510, 2009.

903 Forster, C. B., and Evans, J. P.: Hydrogeology of thrust faults and crystalline thrust sheets: Results of
904 combined field and modeling studies, *Geophysical Research Letters*, 18, 979-982, 1991.

905 Garven, G.: Continental-scale groundwater flow and geologic processes, *Annual Review of Earth and*
906 *Planetary Sciences*, 23, 89-117, 1995.

907 Ghisetti, F., and Vezzani, L.: Normal faulting, extension and uplift in the outer thrust belt of the central
908 Apennines (Italy): role of the Caramanico fault, *Basin Research*, 14, 225-236, 2002.

909 Gonzalez, E., Ferket, H., Callot, J.-P., Guilhaumou, N., Ortuno, F., and Roure, F.: Paleoburial,
910 hydrocarbon generation and migration in the Cordoba platform and Veracruz basin: Insights from fluid
911 inclusion studies and 2D-modelling, *SEPM Special Publication*, 103, 167 - 186, 2013.

912 Grohmann, C. H., and Campanha, G.: OpenStereo: open source, cross-platform software for structural
913 geology analysis, *AGU Fall Meeting abstracts*, 2010,

914 Hitchon, B., and Friedman, I.: Geochemistry and origin of formation waters in the western Canada
915 sedimentary basin—I. Stable isotopes of hydrogen and oxygen, *Geochimica et Cosmochimica Acta*, 33,
916 1321-1349, 1969.

917 Hoareau, G., Claverie, F., Pecheyran, C., Paroissin, C., Grignard, P. A., Motte, G., Chailan, O., and Girard,
918 J. P.: Direct U-Pb dating of carbonates from micron scale fsLA-ICPMS images using robust regression,
919 *Geochronology Discuss.*, 2020, 1-23, 10.5194/gchron-2020-10, 2020.

920 Holl, J. E., and Anastasio, D. J.: Paleomagnetically derived folding rates, southern Pyrenees, Spain,
921 *Geology*, 21, 271-274, 1993.

922 John, C. M., and Bowen, D.: Community software for challenging isotope analysis: First applications of
923 'Easotope' to clumped isotopes, *Rapid Communications in Mass Spectrometry*, 30, 2285-2300, 2016.

924 Kim, S.-T., and O'Neil, J. R.: Equilibrium and nonequilibrium oxygen isotope effects in synthetic
925 carbonates, *Geochimica et Cosmochimica Acta*, 61, 15, 1997.

926 Kim, S.-T., Mucci, A., and Taylor, B. E.: Phosphoric acid fractionation factors for calcite and aragonite
927 between 25 and 75 C: revisited, *Chemical Geology*, 246, 135-146, 2007.

928 Koehn, D., Renard, F., Toussaint, R., and Passchier, C.: Growth of stylolite teeth patterns depending on
929 normal stress and finite compaction, *Earth and Planetary Science Letters*, 257, 582-595,
930 10.1016/j.epsl.2007.03.015, 2007.

931 Koehn, D., Ebner, M., Renard, F., Toussaint, R., and Passchier, C. W.: Modelling of stylolite geometries
932 and stress scaling, *Earth and Planetary Science Letters*, 341-344, 104-113, 10.1016/j.epsl.2012.04.046,
933 2012.

934 Lacombe, O.: Calcite twins, a tool for tectonic studies in thrust belts and stable orogenic forelands, *Oil
935 & Gas Science and Technology—Revue d'IFP Energies nouvelles*, 65, 809-838, 2010.

936 Lacombe, O., Bellahsen, N., and Mouthereau, F.: Fracture patterns in the Zagros Simply Folded Belt
937 (Fars, Iran): constraints on early collisional tectonic history and role of basement faults, *Geological
938 Magazine*, 148, 940-963, 10.1017/s001675681100029x, 2011.

939 Lacombe, O.: Do fault slip data inversions actually yield "paleostresses" that can be compared with
940 contemporary stresses? A critical discussion, *Comptes Rendus Geoscience*, 344, 159-173, 2012.

941 Lacombe, O., Swennen, R., and Caracausi, A.: An introduction to the Special Issue of Marine and
942 Petroleum Geology: Fluid-rock-tectonics interactions in basins and orogens, *Marine and Petroleum
943 Geology*, 55, 1-5, 2014.

944 Lacombe, O., and Bellahsen, N.: Thick-skinned tectonics and basement-involved fold-thrust belts:
945 insights from selected Cenozoic orogens, *Geological Magazine*, 153, 763-810,
946 10.1017/s0016756816000078, 2016.

947 Lacombe, O., and Rolland, Y.: An introduction to the Special Issue: Fluids in crustal deformation: Fluid
948 flow, fluid-rock interactions, rheology, melting and resources, *Journal of Geodynamics*, 101, 1-4, 2016.

949 Lacroix, B., Buatier, M., Labaume, P., Travé, A., Dubois, M., Charpentier, D., Ventalon, S., and Convert-
950 Gaubier, D.: Microtectonic and geochemical characterization of thrusting in a foreland basin: Example
951 of the South-Pyrenean orogenic wedge (Spain), *Journal of Structural Geology*, 33, 1359-1377,
952 10.1016/j.jsg.2011.06.006, 2011.

953 Laubach, S. E., Eichhubl, P., Hilgers, C., and Lander, R. H.: Structural diagenesis, *Journal of Structural
954 Geology*, 32, 1866-1872, 10.1016/j.jsg.2010.10.001, 2010.

955 Laubach, S. E., Lander, R., Criscenti, L. J., Anovitz, L. M., Urai, J., Pollyea, R., Hooker, J. N., Narr, W.,
956 Evans, M. A., and Kerisit, S. N.: The role of chemistry in fracture pattern development and
957 opportunities to advance interpretations of geological materials, *Reviews of Geophysics*, 57, 1065-
958 1111, 2019.

959 Lavecchia, G.: The Tyrrhenian-Apennines system: structural setting and seismotectogenesis,
960 *Tectonophysics*, 147, 263-296, 1988.

961 Lefticariu, L., Perry, E. C., Fischer, M. P., and Banner, J. L.: Evolution of fluid compartmentalization in a
962 detachment fold complex, *Geology*, 33, 69-72, 2005.

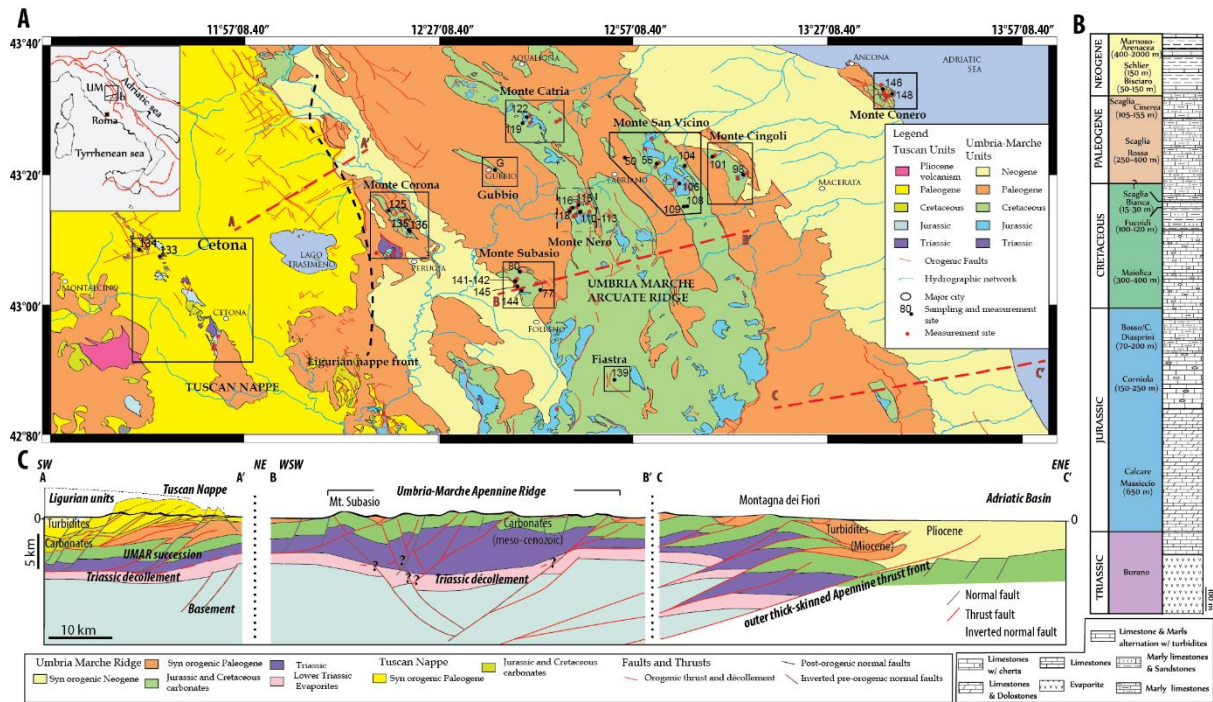
963 Lucca, A., Storti, F., Balsamo, F., Clemenzi, L., Fondriest, M., Burgess, R., and Toro, G. d.: From
964 Submarine to Subaerial Out-of-Sequence Thrusting and Gravity-Driven Extensional Faulting: Gran
965 Sasso Massif, Central Apennines, Italy, *tectonics*, 38, 4155-4184, 10.1029/2019TC005783, 2019.

966 Machel, H. G., and Cavell, P. A.: Low-flux, tectonically-induced squeegee fluid flow, *Bulletin of
967 Canadian Petroleum Geology*, 47, 510-533, 1999.

968 Manger, G. E.: Porosity and bulk density of sedimentary rocks, USGS Bulletin, 1144-E, 55, 1963.
969 Masferro, J. L., Bulnes, M., Poblet, J., and Eberli, G. P.: Episodic folding inferred from syntectonic
970 carbonate sedimentation: the Santaren anticline, Bahamas foreland, *Sedimentary Geology*, 146, 11-
971 24, 2002.
972 Mazzoli, S., Deiana, G., Galdenzi, S., and Cello, G.: Miocene fault-controlled sedimentation and thrust
973 propagation in the previously faulted external zones of the Umbria-Marche Apennines, Italy, EGU
974 Stephan Mueller Special Publication Series, 1, 195-209, 2002.
975 McArthur, J. M., Howarth, R., and Bailey, T.: Strontium isotope stratigraphy: LOWESS version 3: best
976 fit to the marine Sr-isotope curve for 0–509 Ma and accompanying look-up table for deriving numerical
977 age, *The Journal of Geology*, 109, 155-170, 2001.
978 McCaig, A. M.: Deep fluid circulation in fault zones, *Geology*, 16, 867-870, 1988.
979 Meckler, A. N., Ziegler, M., Millán, M. I., Breitenbach, S. F., and Bernasconi, S. M.: Long-term
980 performance of the Kiel carbonate device with a new correction scheme for clumped isotope
981 measurements, *Rapid Communications in Mass Spectrometry*, 28, 1705-1715, 2014.
982 Mirabella, F., Barchi, M., Lupattelli, A., Stucchi, E., and Ciaccio, M.: Insights on the seismogenic layer
983 thickness from the upper crust structure of the Umbria-Marche Apennines (central Italy), *Tectonics*,
984 27, TC1010, 2008.
985 Mozafari, M., Swennen, R., Balsamo, F., Desouky, H. E., Storti, F., and Taberner, C.: Fault-controlled
986 dolomitization in the Montagna dei Fiori Anticline (Central Apennines, Italy): record of a dominantly
987 pre-orogenic fluid migration, *solid earth*, 10, 1355-1383, 10.5194/SE-10-1355-2019, 2019.
988 Muller, I. A., Violay, M. E. S., Storck, J. C., Fernandez, A., van Dijk, J., Madonna, C., and Bernasconi, S.
989 M.: Clumped isotope fractionation during phosphoric acid digestion of carbonates at 70 degrees C,
990 *Chemical Geology*, 449, 1-14, 10.1016/j.chemgeo.2016.11.030, 2017.
991 Oliver, J.: Fluids expelled tectonically from orogenic belts: Their role in hydrocarbon migration and
992 other geologic phenomena, *Geology*, 14, 99-102, 1986.
993 Petracchini, L., Antonellini, M., Billi, A., and Scrocca, D.: Fault development through fractured pelagic
994 carbonates of the Cingoli anticline, Italy: Possible analog for subsurface fluid-conductive fractures,
995 *Journal of Structural Geology*, 45, 21-37, 10.1016/j.jsg.2012.05.007, 2012.
996 Qing, H., and Mountjoy, E.: Large-scale fluid flow in the Middle Devonian Presqu'ile Barrier, Western
997 Canada sedimentary basin, *Geology*, 20, 903-906, 1992.
998 Quintà, A., and Tavani, S.: The foreland deformation in the south-western Basque–Cantabrian Belt
999 (Spain), *Tectonophysics*, 576, 4-19, 2012.
1000 Reynolds, S. J., and Lister, G. S.: Structural aspects of fluid-rock interactions in detachment zones,
1001 *Geology*, 15, 362-366, 1987.
1002 Roberts, N. M., and Walker, R. J.: U-Pb geochronology of calcite-mineralized faults: Absolute timing of
1003 rift-related fault events on the northeast Atlantic margin, *Geology*, 44, 531-534, 2016.
1004 Roberts, N. M., Rasbury, E. T., Parrish, R. R., Smith, C. J., Horstwood, M. S., and Condon, D. J.: A calcite
1005 reference material for LA-ICP-MS U-Pb geochronology, *Geochem Geophys Geosyst*, 18, 2807-2814,
1006 2017.
1007 Roberts, N. M. W., Drost, K., Horstwood, M. S. A., Condon, D. J., Chew, D., Drake, H., Milodowski, A.
1008 E., McLean, N. M., Smye, A. J., Walker, R. J., Haslam, R., Hodson, K., Imber, J., Beaudoin, N., and Lee, J.
1009 K.: Laser ablation inductively coupled plasma mass spectrometry (LA-ICP-MS) U–Pb carbonate
1010 geochronology: strategies, progress, and limitations, *Geochronology*, 2, 33-61, 10.5194/gchron-2-33-
1011 2020, 2020.
1012 Rolland, A., Toussaint, R., Baud, P., Schmittbuhl, J., Conil, N., Koehn, D., Renard, F., and Gratier, J.-P.:
1013 Modeling the growth of stylolites in sedimentary rocks, *Journal of Geophysical Research: Solid Earth*,
1014 117, B06403, 10.1029/2011jb009065, 2012.
1015 Rolland, A., Toussaint, R., Baud, P., Conil, N., and Landrein, P.: Morphological analysis of stylolites for
1016 paleostress estimation in limestones, *International Journal of Rock Mechanics and Mining Sciences*,
1017 67, 212-225, 10.1016/j.ijrmms.2013.08.021, 2014.

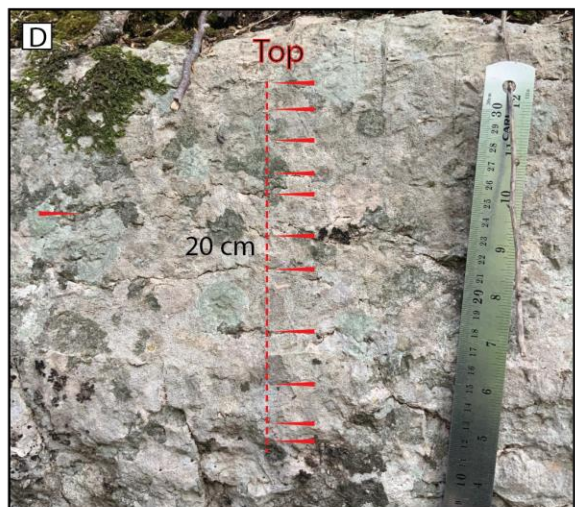
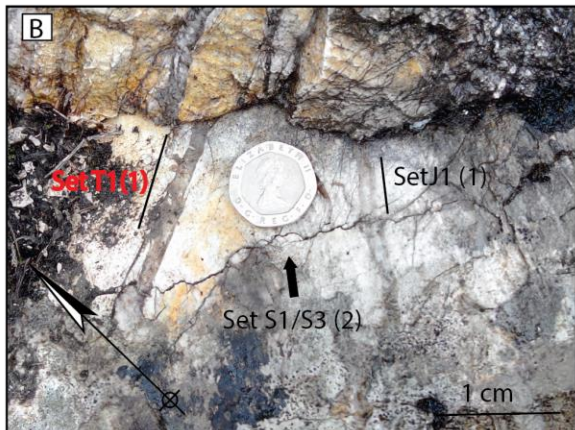
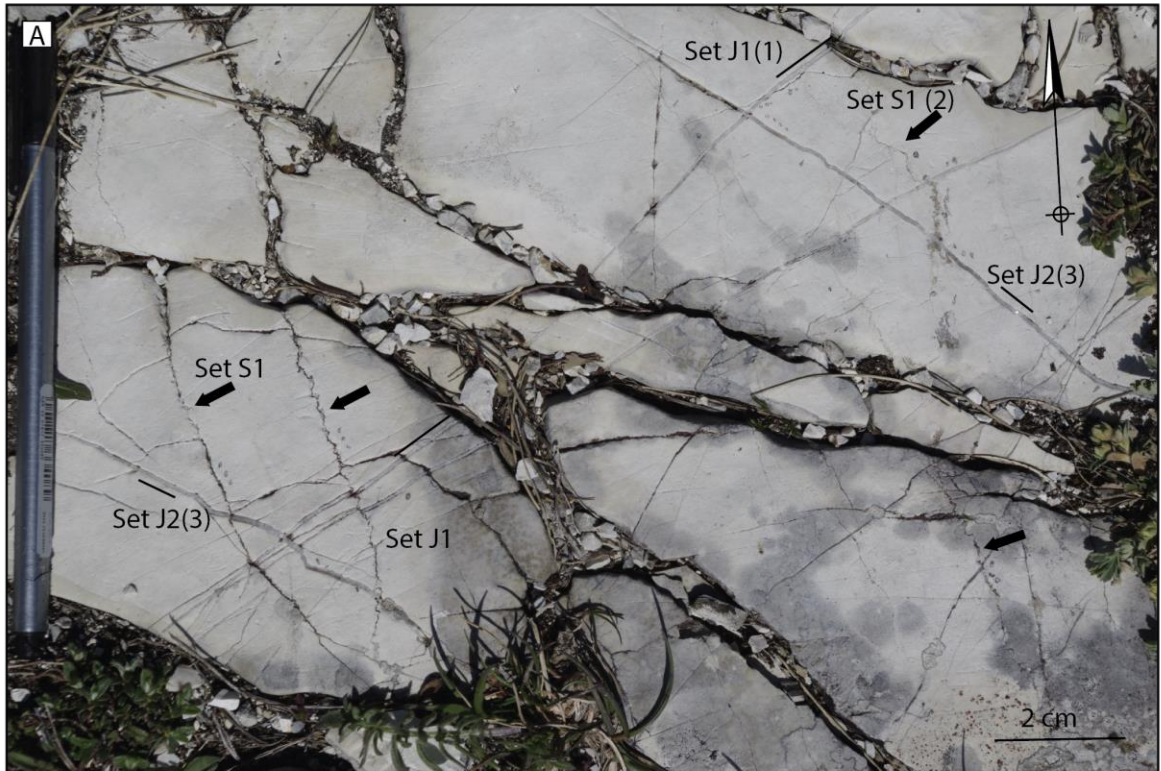
1018 Roure, F., Bordas-Lefloch, N., Toro, J., Aubourg, C., Guilhaumou, N., Hernandez, E., Lecornec-Lance, S.,
1019 Rivero, C., Robion, P., and Sassi, W.: Petroleum systems and reservoir appraisal in the sub-Andean
1020 basins (eastern Venezuela and eastern Colombian foothills), *AAPG Memoirs*, 79, 750-775, 2003.
1021 Roure, F., Swennen, R., Schneider, F., Faure, J., Ferket, H., Guilhaumou, N., Osadetz, K., Robion, P., and
1022 Vandeginste, V.: Incidence and importance of tectonics and natural fluid migration on reservoir
1023 evolution in foreland fold-and-thrust belts, *Oil & Gas Science and Technology*, 60, 67-106, 2005.
1024 Roure F., Andriessen P., Callot J.-P., Ferket H., Gonzalez E., Guilhaumou N., Hardebol N., Lacombe O.,
1025 Malandain J., Mougou P., Muska K., Ortuno S., Sassi W., Swennen R., and Vilasi N.: The use of paleo-
1026 thermo-barometers and coupled thermal, fluid flow and pore fluid pressure modelling for
1027 hydrocarbon and reservoir prediction in fold-and-thrust belts. In "Hydrocarbons in Contractual
1028 Belts", Geological Society, London, Special Publications, 348, 87-114, 2010, doi:10.1144/SP348.6
1029 Sassi, W., Guiton, M., Leroy, Y., Daniel, J.-M., and Callot, J.-P.: Constraints on bed scale fracture
1030 chronology with a FEM mechanical model of folding: The case of Split Mountain (Utah, USA),
1031 *Tectonophysics*, 576, 197-215, 2012.
1032 Schmittbuhl, J., Renard, F., Gratier, J. P., and Toussaint, R.: Roughness of stylolites: implications of 3D
1033 high resolution topography measurements, *Phys Rev Lett*, 93, 238501,
1034 10.1103/PhysRevLett.93.238501, 2004.
1035 Schneider, F., Faure, J., and Roure, F.: Methodology for basin modeling in complex area: examples
1036 from Eastern Venezuelan and Canadian Foothills, *AAPG Hedberg Conference "Deformation History,
1037 Fluid Flow Reconstruction and Reservoir Appraisal in Foreland Fold and Thrust Belts 2002*, 14-18,
1038 Schneider, F., Pagel, M., and Hernandez, E.: Basin modeling in a complex area: Example from the
1039 Eastern Venezuelan foothills, in: *Deformation, fluid flow, and reservoir appraisal in foreland fold and
1040 thrust belts: AAPG Hedberg Series*, edited by: Swennen, R., Roure, F., and Granath, J. W., 357-369,
1041 2004.
1042 Scisciani, V., Agostini, S., Calamita, F., Pace, P., Cilli, A., Giori, I., and Paltrinieri, W.: Positive inversion
1043 tectonics in foreland fold-and-thrust belts: a reappraisal of the Umbria–Marche Northern Apennines
1044 (Central Italy) by integrating geological and geophysical data, *Tectonophysics*, 637, 218-237, 2014.
1045 Scisciani, V., Patruno, S., Tavarnelli, E., Calamita, F., Pace, P., and Iacopini, D.: Multi-phase reactivations
1046 and inversions of Paleozoic–Mesozoic extensional basins during the Wilson cycle: case studies from
1047 the North Sea (UK) and the Northern Apennines (Italy), *Geological Society, London, Special
1048 Publications*, 470, 205-243, 10.1144/sp470-2017-232, 2019.
1049 Simonsen, I., Hansen, A., and Nes, O. M.: Determination of the Hurst exponent by use of wavelet
1050 transforms, *Physical Review E*, 58, 2779, 1998.
1051 Smith, A. P., Fischer, M. P., and Evans, M. A.: Fracture-controlled palaeohydrology of a secondary salt
1052 weld, La Popa Basin, NE Mexico, *Geological Society, London, Special Publications*, 363, 107-130, 2012.
1053 Stearns, D. W., and Friedman, M.: *Reservoirs in fractured rock: Geologic exploration methods*, 1972.
1054 Storti, F., Balsamo, F., Mozafari, M., Koopman, A., Swennen, R., and Taberner, C.: Syn-Contractual
1055 Overprinting Between Extension and Shortening Along the Montagna Dei Fiori Fault During Plio-
1056 Pleistocene Antiformal Stacking at the Central Apennines Thrust Wedge Toe, *Tectonics*, 37, 3690-
1057 3720, 10.1029/2018tc005072, 2018.
1058 Suppe, J., Chou, G. T., and Hook, S. C.: Rates of folding and faulting determined from growth strata, in:
1059 *Thrust tectonics*, Springer, 105-121, 1992.
1060 Tavani, S., Storti, F., Salvini, F., and Toscano, C.: Stratigraphic versus structural control on the
1061 deformation pattern associated with the evolution of the Mt. Catria anticline, Italy, *Journal of
1062 Structural Geology*, 30, 664-681, 10.1016/j.jsg.2008.01.011, 2008.
1063 Tavani, S., and Cifelli, F.: Deformation pattern analysis and tectonic implications of a décollement level
1064 within the Central Apennines (Italy), *Geological Journal*, 45, 582-596, 10.1002/gj.1198, 2010.
1065 Tavani, S., Storti, F., Bausà, J., and Muñoz, J. A.: Late thrusting extensional collapse at the mountain
1066 front of the northern Apennines (Italy), *Tectonics*, 31, TC4019, 10.1029/2011tc003059, 2012.

- 1067 Tavani, S., Storti, F., Lacombe, O., Corradetti, A., Muñoz, J., and Mazzoli, S.: A review of deformation
1068 pattern templates in foreland basin systems and fold-and-thrust belts: Implications for the state of
1069 stress in the frontal regions of thrust wedges, *Earth-Science Reviews*, 141, 82-104, 2015.
- 1070 Tavarnelli, E., Butler, R., Decandia, F., Calamita, F., Grasso, M., Alvarez, W., Renda, P., Crescenti, U.,
1071 and D'offizi, S.: Implications of fault reactivation and structural inheritance in the Cenozoic tectonic
1072 evolution of Italy, *The Geology of Italy, Special*, 1, 209-222, 2004.
- 1073 Toussaint, R., Aharonov, E., Koehn, D., Gratier, J. P., Ebner, M., Baud, P., Rolland, A., and Renard, F.:
1074 Stylolites: A review, *Journal of Structural Geology*, 114, 163-195, 10.1016/j.jsg.2018.05.003, 2018.
- 1075 Travé, A., Calvet, F., Sans, M., Vergés, J., and Thirlwall, M.: Fluid history related to the Alpine
1076 compression at the margin of the south-Pyrenean Foreland basin: the El Guix anticline,
1077 *Tectonophysics*, 321, 73-102, 2000.
- 1078 Travé, A., Labaume, P., and Vergés, J.: Fluid systems in foreland fold-and-thrust belts: an overview
1079 from the Southern Pyrenees, in: *Thrust belts and foreland basins*, Springer, 93-115, 2007.
- 1080 Van Geet, M., Swennen, R., Durmishi, C., Roure, F., and Muchez, P.: Paragenesis of Cretaceous to
1081 Eocene carbonate reservoirs in the Ionian fold and thrust belt (Albania): relation between tectonism
1082 and fluid flow, *Sedimentology*, 49, 697-718, 2002.
- 1083 Vandeginste, V., Swennen, R., Allaey, M., Ellam, R. M., Osadetz, K., and Roure, F.: Challenges of
1084 structural diagenesis in foreland fold-and-thrust belts: a case study on paleofluid flow in the Canadian
1085 Rocky Mountains West of Calgary, *Marine and Petroleum Geology*, 35, 235-251, 2012.
- 1086 Vannucchi, P., Remitti, F., Bettelli, G., Boschi, C., and Dallai, L.: Fluid history related to the early Eocene-
1087 middle Miocene convergent system of the Northern Apennines (Italy): Constraints from structural and
1088 isotopic studies, *Journal of geophysical research*, 115, 10.1029/2009JB006590, 2010.
- 1089 Vass, A., Koehn, D., Toussaint, R., Ghani, I., and Piazzolo, S.: The importance of fracture-healing on the
1090 deformation of fluid-filled layered systems, *Journal of Structural Geology*, 67, 94-106,
1091 10.1016/j.jsg.2014.07.007, 2014.
- 1092 Vignaroli, G., Pinton, A., De Benedetti, A. A., Giordano, G., Rossetti, F., Soligo, M., and Berardi, G.:
1093 Structural compartmentalisation of a geothermal system, the Torre Alfina field (central Italy),
1094 *Tectonophysics*, 608, 482-498, 2013.
- 1095 Vilasi, N., Malandain, J., Barrier, L., Callot, J.-P., Amrouch, K., Guilhaumou, N., Lacombe, O., Muska, K.,
1096 Roure, F., and Swennen, R.: From outcrop and petrographic studies to basin-scale fluid flow modelling:
1097 The use of the Albanian natural laboratory for carbonate reservoir characterisation, *Tectonophysics*,
1098 474, 367-392, 2009.
- 1099 Watts, A. B.: *Isostasy and Flexure of the Lithosphere*, Cambridge University Press, 458 pp., 2001.
- 1100 Wright, K., Cygan, R. T., and Slater, B.: Structure of the (101 [combining macron] 4) surfaces of calcite,
1101 dolomite and magnesite under wet and dry conditions, *Physical Chemistry Chemical Physics*, 3, 839-
1102 844, 2001.
- 1103 Yamato, P., Kaus, B. J., Mouthereau, F., and Castelltort, S.: Dynamic constraints on the crustal-scale
1104 rheology of the Zagros fold belt, Iran, *Geology*, 39, 815-818, 2011.
- 1105 Figures with captions

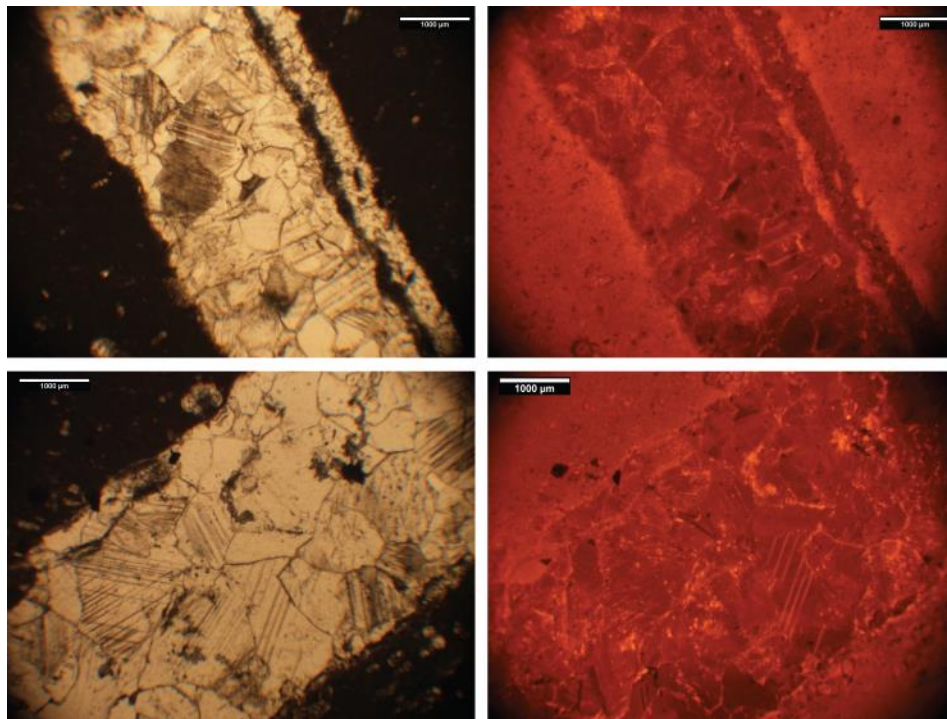


1106

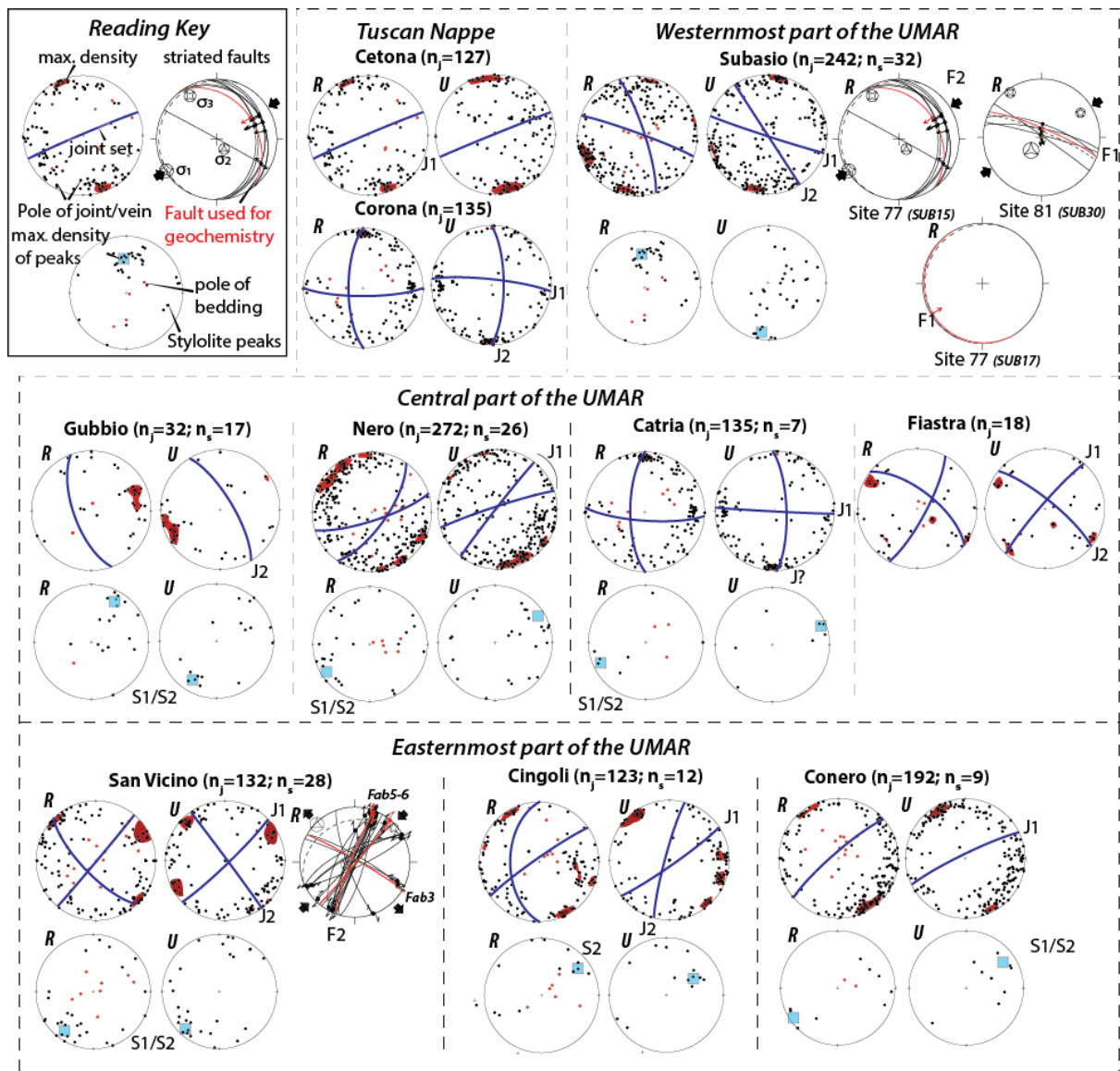
1107 Figure 1: Simplified geological map of the study area, with locations of the sampling and measurement
 1108 sites. Frames relate to the fracture study areas used in figure 4. Exact location of measurement sites
 1109 is reported as black and red points, and labelled black points also represent the sampling sites for
 1110 geochemical analysis. B. Stratigraphic column based on stratigraphic and well data from the central
 1111 part of the UMAR, after Centamore et al. (1979). C. Crustal-scale composite cross-section based on
 1112 published seismic data interpretations, A-A' modified after Carboni et al. (2020); B-B' and C-C' after
 1113 Scisciani et al. (2014). Note that both tectonic style (thick-skinned and thin-skinned) are represented
 1114 by question marks for the UMAR.



1116 Figure 2: Field photographs showing chronological relationships between veins/joints and stylolites.
1117 a) Monte Nero, b) Monte Cingoli, Sets are reported along with local chronological order between
1118 brackets. Bedding-parallel stylolites spacing from c) the Maiolica Fm. (Monte Subasio) and d) the
1119 Massiccio Fm. (Monte Cingoli). Intersections between BPS and scanline are pointed out with red
1120 arrows.

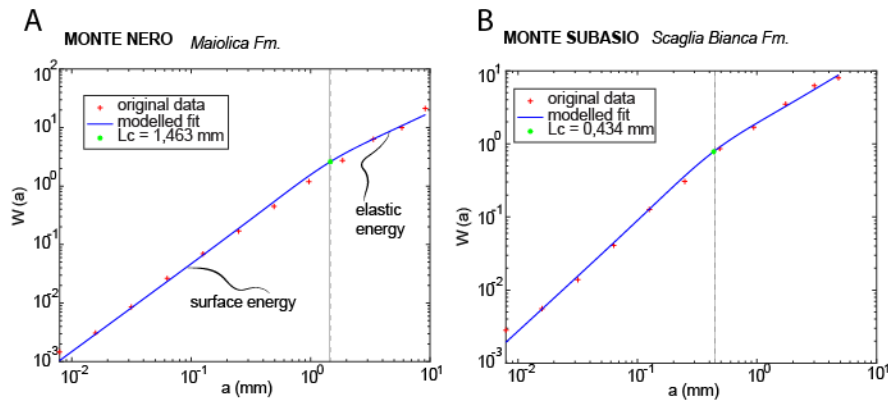


1121
1122 Figure 3: photomicrographs of various veins in plain polarized light (left-hand side), with
1123 corresponding view under cathodoluminescence (right-hand side), top one is a set J1 vein from the
1124 Scaglia Fm., bottom one is a set J2 from the Maiolica Fm.



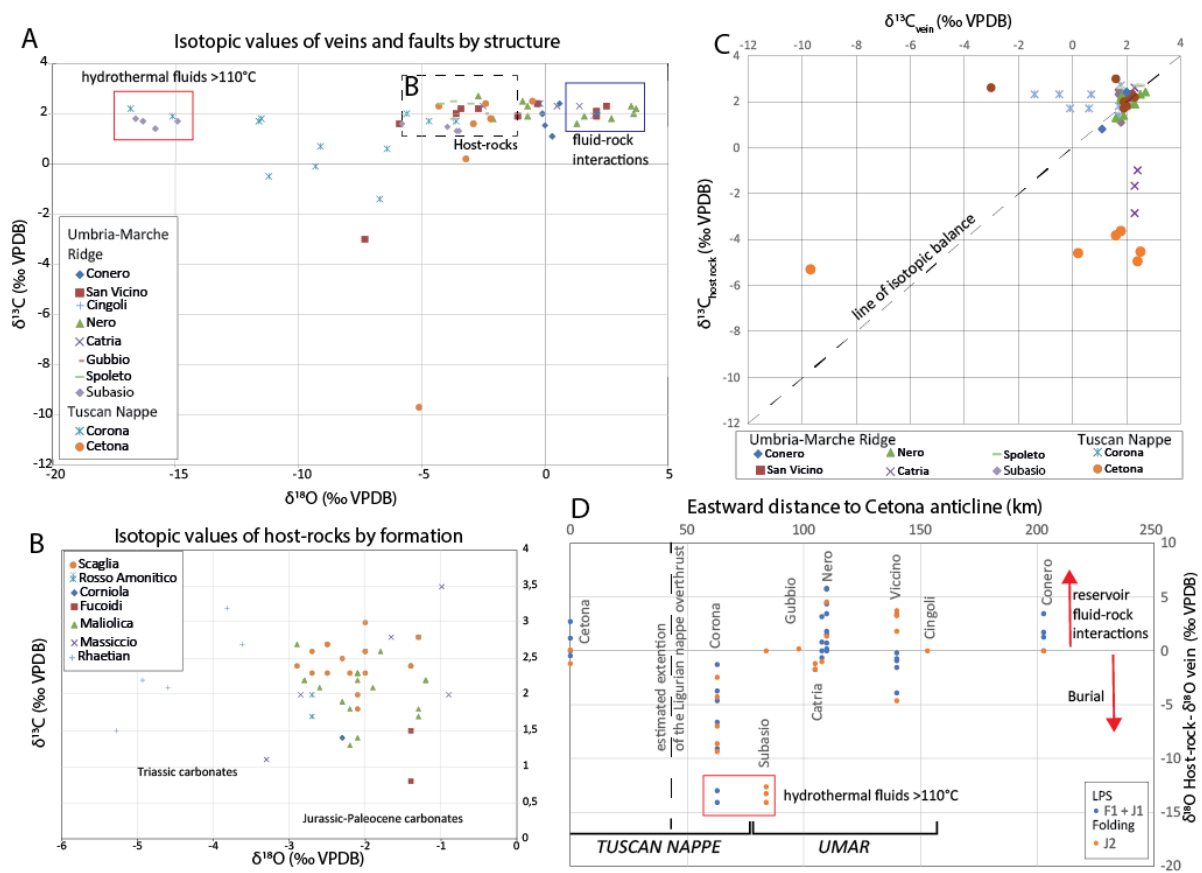
1125

1126 Figure 4: Poles of measured joints/veins and stylolite peaks projected on Schmidt stereograms, lower
 1127 hemisphere, for the different structures. Data are projected in the current attitude of the strata (left,
 1128 R), with pole to bedding in red, and after unfolding (right, U). Red areas represent highest density
 1129 according to Fischer statistical analysis using the software OpenStereo, and main fracture set average
 1130 orientations are represented as blue planes. For tectonic stylolite peaks, the blue square represents
 1131 highest density according to Fischer statistical analysis. Striated fault inversion results are reported in
 1132 the current attitude of the strata (bedding as dashed line).



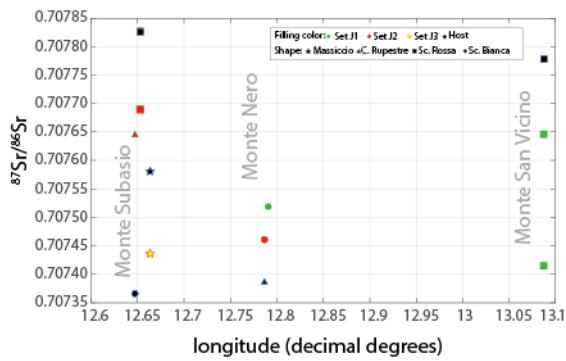
1133

1134 Figure 5: Examples of results of stylolite roughness inversion, with signal analysis by Average Wavelet
 1135 in the Monte Nero (A) and in the Monte Subasio (B).



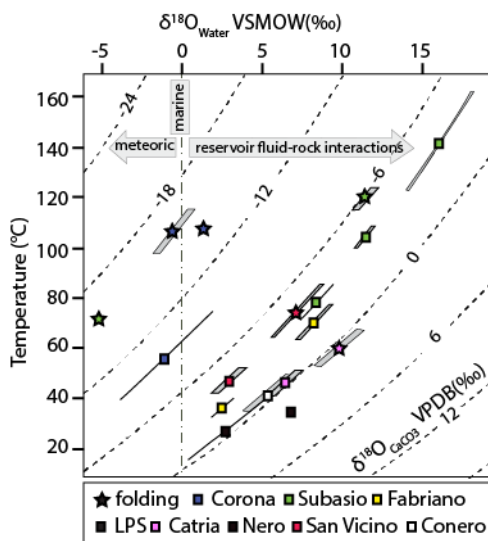
1136

1137 Figure 6: A) Plot of $\delta^{13}\text{C}$ vs $\delta^{18}\text{O}$ (% VPDB) of veins represented by structure. Frames represent the
 1138 different type of fluid system. B) Plot of $\delta^{13}\text{C}$ vs $\delta^{18}\text{O}$ (% VPDB) of host-rocks represented by structure.
 1139 C) Plot of $\delta^{13}\text{C}_{\text{vein}}$ vs $\delta^{13}\text{C}_{\text{host}}$ (% VPDB) of veins represented by structures. D) Plot of the difference
 1140 between $\delta^{18}\text{O}$ of host-rocks and $\delta^{18}\text{O}$ of veins (% VPDB) vs eastward distance from the Cetona
 1141 Anticline towards the Adriatic basin across the strike of the UMAR. Data are represented by tectonic
 1142 sets. The proposed extension of the Ligurian nappe overthrust is reported after Caricchi et al., (2014);
 1143 red frames and arrows represent the fluid systems.



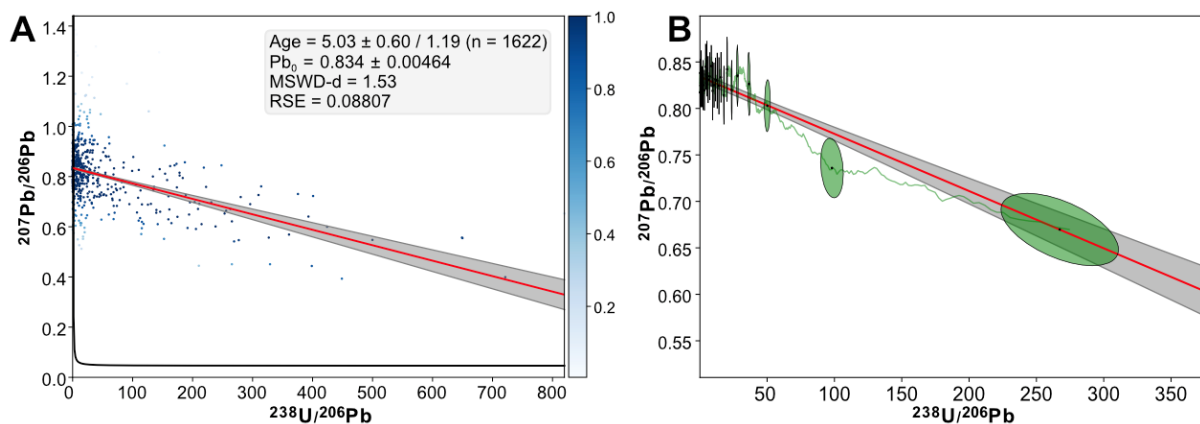
1144

1145 Figure 7: Plot of $^{87}\text{Sr}/^{86}\text{Sr}$ values vs longitude, with filling color related to tectonic set and point shape
 1146 related to host rock formation. Note that the host-rock values are equivalent to the related formation
 1147 seawater values.



1148

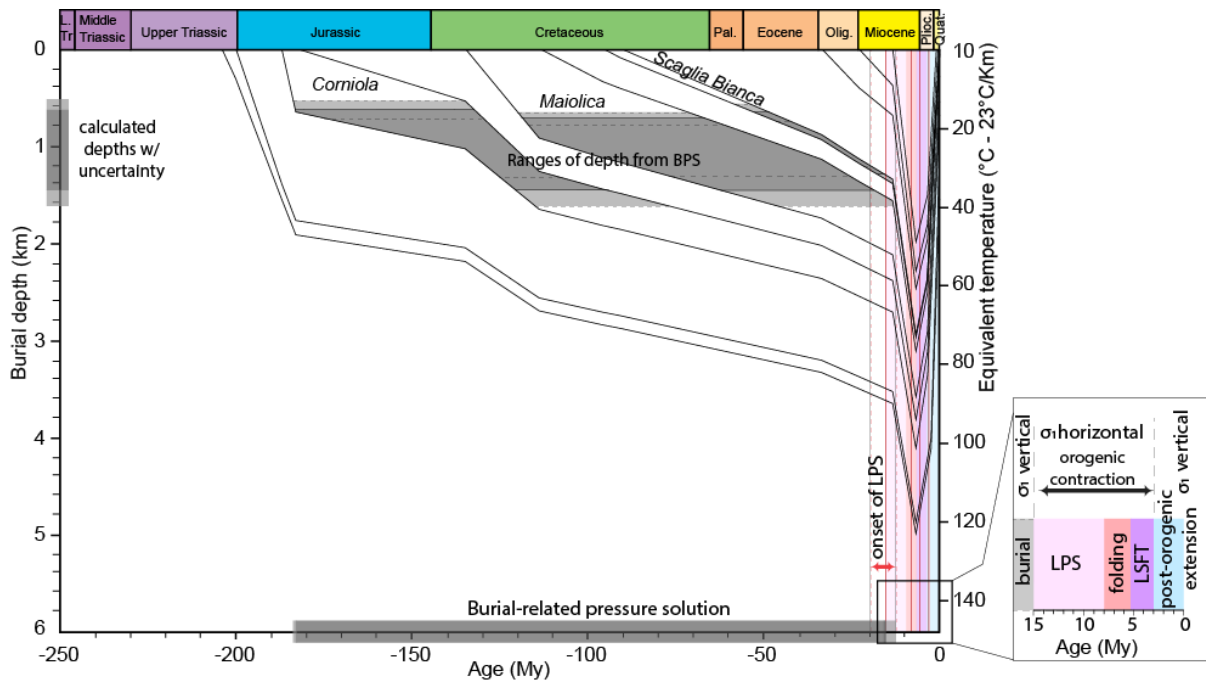
1149 Figure 8: Plot of $\delta^{18}\text{O}_{\text{fluid}}$ (‰ SMOW) vs precipitation temperature ($^{\circ}\text{C}$) obtained from clumped isotope
 1150 analyses along with uncertainties reported as greyed contours. Dotted oblique lines are the measured
 1151 $\delta^{18}\text{O}_{\text{CaCO}_3}$ of the vein cements (‰ PDB). Shape of the points correspond to tectonic set (LPS being U1
 1152 and compatible faults and folding U2), while filling color relates to structure.



1153

1154 Fig. 9: A) Tera-Wasserburg concordia plot obtained from LA-ICPMS U-Pb dating of FAB5 calcite sample.
 1155 The age was obtained by robust regression through the U-Pb image pixel values. The scale bar
 1156 corresponds to the weight of each pixel as determined by robust regression. B) Same plot but with

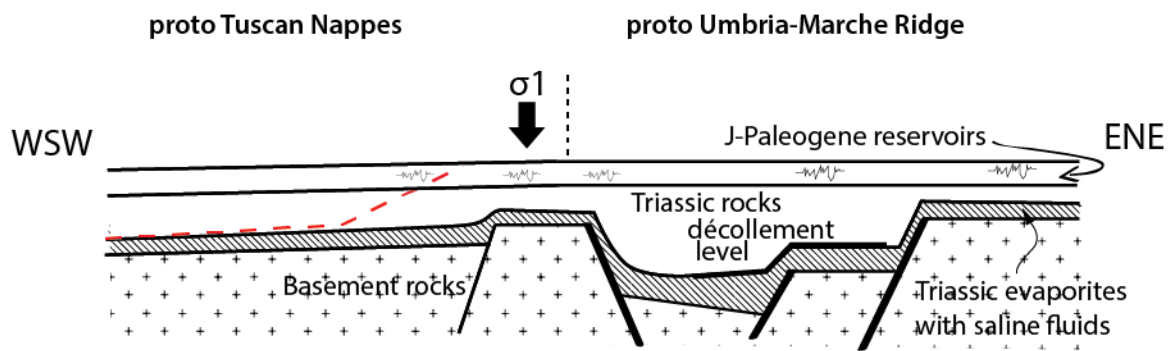
1157 discretized data represented as ellipses (one ellipse = 60 pixels). The running mean (window = 60
 1158 pixels) is also shown as green line.



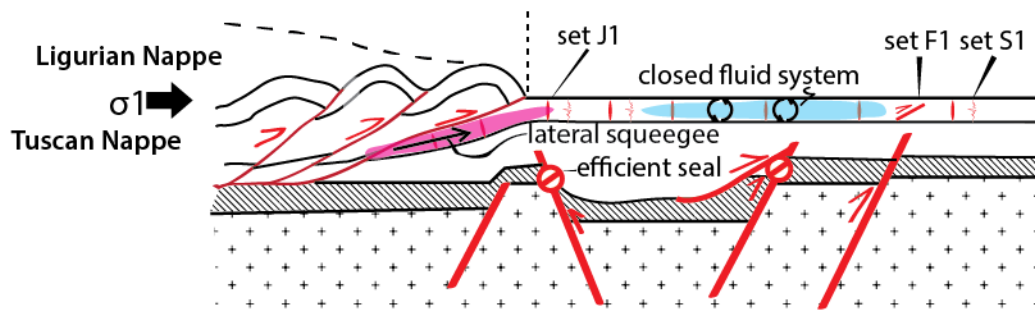
1159

1160 Figure 10: Burial model constructed considering thickness from well data (central UMAR)
 1161 from both chemical and physical compaction. The range of depths reconstructed from bedding parallel
 1162 stylolite roughness inversion (with uncertainty) are reported for each formation as grey shades. The
 1163 derived corresponding timing and depth of active dissolution are reported on the x-axis and left y-axis,
 1164 respectively. The timing of the deformation is reported on the right-hand side in the inset. The onset
 1165 of Layer Parallel shortening is deduced from the latest bedding stylolite to have been active, the effect
 1166 of the 12% uncertainty is represented by dashed red lines, the onset of LSFT is given by U-Pb dating of
 1167 fault coating in this study. The timing of folding and post-orogenic extension are reported from
 1168 published sedimentary data (see text for more detailed explanations).

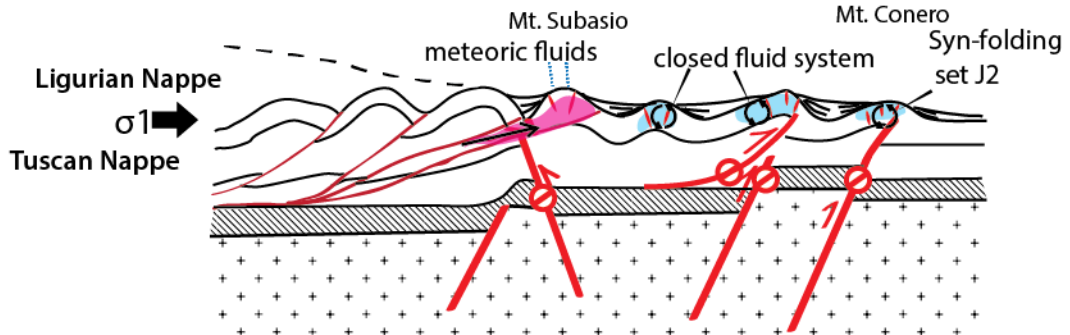
a) Burial up to Burdigalian - Serravalian (15 +/- 3 Ma)



b) LPS in the UMAR from Serravalian to Tortonian (~8Ma)



c) Folding in the UMAR from Tortonian to ~Messinian (5.5 Ma)



1169

1170 Figure 11: Conceptual model representing fracture development and regional scale fluid migration
 1171 during the formation of the Tuscan Nappes and Umbria Marche Ridge. Red areas represent the extent
 1172 of eastward pulses of hydrothermal fluids. Blue areas represent closed fluid system at the scale of the
 1173 carbonate reservoirs. Potential effects of flexural event reported during upper Burdigalian and Lower
 1174 Messinian in the eastern part of the belt (Mazzoli et al., 2002; Tavani et al., 2012) has not been
 1175 documented in our dataset therefore is not considered in this scenario.

1176

1177

1178

1179

1180

1181

1182

1183 Table 1 - Results of Stylolite Roughness Inversion applied on bedding-parallel stylolites

Sample	GPS	location	formation	Dissolution (mm)	Lc (mm)*	E (GPa)	mu	v	vertstress (Pa)	depth (m)
A165	165	Subasio	Scaglia Bianca	2,7	1,059	23,2	0,25	0,32	21811000	926
	165	Subasio	Scaglia Bianca	2,0	1,306	23,2	0,25	0,32	19640000	834
	165	Subasio	Scaglia Bianca	0,6	0,46	23,2	0,25	0,32	33093000	1406
	165	Subasio	Scaglia Bianca	0,5	0,486	23,2	0,25	0,32	32196000	1368
	165	Subasio	Scaglia Bianca	1,3	0,434	23,2	0,25	0,32	34070000	1447
	165	Subasio	Scaglia Bianca	3,1	0,971	23,2	0,25	0,32	22778000	967
	165	Subasio	Scaglia Bianca	1,3	1,488	23,2	0,25	0,32	18400000	782
AN26	110	Nero	Maiolica	3,1	1,073	23,2	0,25	0,32	21668000	920
	110	Nero	Maiolica	2,8	1,535	23,2	0,25	0,32	18116000	769
	110	Nero	Maiolica	1,7	1,463	23,2	0,25	0,32	18557000	788
	110	Nero	Maiolica	2,2	1,071	23,2	0,25	0,32	21688000	921
	110	Nero	Maiolica	3,0	1,29	23,2	0,25	0,32	19762000	839
	110	Nero	Maiolica	2,2	1,073	23,2	0,25	0,32	22661000	962
	110	Nero	Maiolica	1,8	1,596	23,2	0,25	0,32	17767000	755
	110	Nero	Maiolica	6,4	0,659	23,2	0,25	0,32	27649000	1174
AN16	115	Nero	Maiolica	2,7	1,279	23,2	0,25	0,32	19847000	843
A137	148	Conero	Scaglia Bianca	5,2	2,073	23,2	0,25	0,32	15589000	662
A123-2	130	Gubbio	Corniola	2,1	0,428	23,2	0,25	0,32	34308000	1457
A123	130	Gubbio	Corniola	1,3	0,791	23,2	0,25	0,32	25237000	1072
	130	Gubbio	Corniola	1,8	2,35	23,2	0,25	0,32	14642000	622
	130	Gubbio	Corniola	2,3	1,457	23,2	0,25	0,32	18595000	790
A21	104	San Vincino	Maiolica	2,1	0,906	23,2	0,25	0,32	23581000	1002
	104	San Vincino	Maiolica	3,4	0,787	23,2	0,25	0,32	25414000	1079
A104	138	Spoletto	Scaglia Bianca	8,5	0,655	23,2	0,25	0,32	27733000	1178
	138	Spoletto	Scaglia Bianca	2,8	0,634	23,2	0,25	0,32	28189000	1197
	138	Spoletto	Scaglia Bianca	0,7	0,66	23,2	0,25	0,32	27628000	1174
	138	Spoletto	Scaglia Bianca	0,6	1,22	23,2	0,25	0,32	20321000	863
	138	Spoletto	Scaglia Bianca	3,4	0,749	23,2	0,25	0,32	25935000	1102
	138	Spoletto	Scaglia Bianca	2,5	1,322	23,2	0,25	0,32	19521000	829

* the crossover length is given within 12% uncertainty, using values for Young Modulus of 23,2 Gpa (Beaudoin et al., 2014), Poisson ratio of 0,25 and an interfacial energy of 0,32 J.m⁻²

1184

1185

1186

1187

1188

1189

1190

1191

1192

1193

1194

1195

1196 Table 2 - Results of stable isotopic analyses of O, C, and ⁸⁷Sr/⁸⁶Sr

Sample	GPS	Formation	Structure	Set	$\delta^{18}\text{O}$ Vein	$\delta^{13}\text{C}$ Vein	$\delta^{18}\text{O}$ HR	$\delta^{13}\text{C}$ HR	⁸⁷ Sr/ ⁸⁶ Sr _v	⁸⁷ Sr/ ⁸⁶ Sr _{HR}
					‰VPDB	‰VPDB	‰VPDB	‰VPDB		
A94V	134	Retian *	Cetona	J1	-3,2	0,2	-3,2	-4,6		
A93V	134	Retian *	Cetona	J1	-2,9	1,6	-2,5	-3,8		
A95V	134	Retian *	Cetona	J1	-0,5	2,5	-3,2	-4,5		
A92V	134	Retian *	Cetona	J1	-4,3	2,3				
A89V	133	Retian *	Cetona	J1	-2,4	2,4	-3,6	-4,9		
A84V	133	Retian *	Cetona	J2	-2,2	1,8	-2,3	-3,6		
A86V	133	Retian *	Cetona	J2	-5,1	-9,7	-3,9	-5,3		
A76F	125	Maliolica	Corona	F1	-6,7	-1,4	-2,1	2,3		
A76V2	125	Maliolica	Corona	J1	-15,1	1,9	-2,1	2,3		
A76V1	125	Maliolica	Corona	J1	-11,2	-0,5	-2,1	2,3		
A72V	125	Maliolica	Corona	J2	-5,6	2,0	-1,3	1,8		
A76V3	125	Maliolica	Corona	J2	-9,1	0,7	-2,1	2,3		
A77V2	125	Maliolica	Corona	J2	-11,6	1,7	-2,2	1,8		
A77V1	125	Maliolica	Corona	J2	-11,5	1,8	-2,9	2,7		
A96V	135	Rosso Amonitico	Corona	J1	-16,8	2,2	-2,7	2,0		
A97bV1	135	Rosso Amonitico	Corona	J1	-6,4	0,6	-2,7	1,7		
A97bV2	135	Rosso Amonitico	Corona	J1	-9,3	-0,1	-2,7	1,7		
A98V1	136	Corniola	Corona	J1	-3,6	1,7	-2,3	1,4		
A98V2	136	Corniola	Corona	J2	-4,7	1,7	-2,3	1,4		
A121V	G	Maliolica	Gubbio	J2	-2,4	2,0	-2,6	2,1		
A112V1	141	Massiccio	Subasio	J2	-15,8	1,4				
A111V	141	Massiccio	Subasio	J2	-16,6	1,8	-3,3	1,1	0,707644	0,707366
A118V	145	Scaglio Rossa	Subasio	J2	-16,3	1,7	-2,2	2,3	0,707690	0,707827
A120V	145	Scaglia Rossa	Subasio	J2	-14,9	1,7	-2,3	2,5		
A116V	144	Massiccio	Subasio	J3					0,707437	0,707580
SUB15	77	Scaglia Cinerea	Subasio	F1	-3,5	1,3				
SUB17	77	Scaglia Cinerea	Subasio	F1	-3,6	1,3				
SUB30	81	Scaglia Cinerea	Subasio	F1	-4,0	1,5				
A28V	106	Massiccio*	Subasio	J1	-5,8	1,6				
A59V	119	Maliolica	Catria	J1	1,4	2,3	-1,8	2,6		
A73V	122	Massiccio*	Catria	J1	-0,2	2,4	0,4	-1,0		
A63V	122	Massiccio*	Catria	J1	0,5	2,3	-0,3	-1,7		
A66V	122	Massiccio*	Catria	J2	-2,5	2,3	-1,5	-2,9		
A65	122	Massiccio*	Catria	J1	2,0	1,9				
A56V	118	Scaglia Cinera	Nero	J1	-0,9	2,5	-2,7	2,3		
A57bV	118	Scaglia Cinera	Nero	J1	-2,7	2,7	-2,9	2,4	0,707461	0,707382
A53V1	116	Maliolica	Nero	J1	-2,1	1,8	-2,8	2,2	0,707519	
A53V2	116	Maliolica	Nero	J1	1,6	1,9	-2,8	2,2		
A52V	115	Maliolica	Nero	J1	1,3	1,6	-2,2	1,3		
A50V1	113	Maliolica	Nero	J1	-0,7	2,3	-2,3	1,9		
A50V2	113	Maliolica	Nero	J1	3,5	2,3	-2,3	1,9		
A47V	112	Maliolica	Nero	J1	3,7	2,2				
A46V	112	Maliolica	Nero	J2	2,7	1,8	-1,9	2,1		
A44V	111	Maliolica	Nero	J1	3,6	2,0	-2,1	2,2		
A43V	110	Maliolica	Nero	J2	-0,7	1,9	-2,1	1,4		
A107F	139	Scaglia Rossa	Spoletto	F1	-4,2	2,4	-2,5	2,7		
A107V	139	Scaglia Rossa	Spoletto	J1	-3,7	2,5	-2,5	2,7		
A104V1	139	Scaglia Rossa	Spoletto	J2	-3,7	1,8	-2,0	2,6		
A27V	106	Massiccio	San Vicinno	J1	-1,1	1,9	-0,9	2,0		
A40F	109	Scaglia Bianca	San Vicinno	F1	-5,9	1,6	-2,0	3,0		
A38V	109	Scaglia Bianca	San Vicinno	J2	-7,3	-3,0	-2,7	2,6	0,707646	0,707778
A18V	104	Maliolica	San Vicinno	J1	2,1	1,9	-1,3	1,7		
A74V1	104	Maliolica	San Vicinno	J2	2,1	2,1	-1,2	2,2		
A74V2	104	Maliolica	San Vicinno	J2	2,5	2,3	-1,2	2,2		
A32V	108	Scaglia Bianca	San Vicinno	J1	-3,4	2,2	-2,5	2,3	0,707415	0,707778
A29V	108	Scaglia Bianca	San Vicinno	J1	-3,6	2,0	-2,1	1,8		
A34V	108	Scaglia Bianca	San Vicinno	J1	-2,7	2,2	-2,0	2,3		
A30V	108	Scaglia Bianca	San Vicinno	J2	-0,3	2,4	-2,1	2,0		
A39V	109	Scaglia Rossa	San Vicinno	J2	-4,1	0,3				
FAB3	50	Langhian Flysh	San Vicinno	F2	-2,5	0,5				
FAB6	50	Langhian Flysh	San Vicinno	F2	-2,5	0,4				
A14V	101	Scaglia	Cingoli	J2			-1,3	2,8		
A129bF	146	Scaglia	Conero	F1	2,1	2,0	-1,4	2,4		
A129bV	146	Scaglia	Conero	F1	-0,1	2,0	-1,4	2,4		
A126V	146	Scaglia	Conero	J2	0,6	2,4				
A133V	148	Fucoidi	Conero	J1			-1,4	1,5		
CON6	68	Scaglia Rossa	Conero	J1	0,0	1,5				
A135V	148	Fucoidi	Conero	J1	0,3	1,1	-1,4	0,8		

*: Values were corrected to reflect the fact that host rocks is dolomite; HR stands for Host Rock, V stands for Vein

1198 Table 3 - Fluid precipitation temperature and oxygen isotopic values derived from clumped isotope
 1199 analysis results

Sample Name	Structure	Set	GPS	Host formation	Mineralogy	Temperature (°C)	MinT (°C)	MaxT (°C)	Fluid δ18O ‰VSMOW (mean)	Fluid δ18O ‰VSMOW (min)	Fluid δ18O ‰VSMOW (max)	Δ47 ‰CDES (Final)	Δ47 ‰CDES (Final) SD
A74A	Corona	J2	125	Maiolica	Calcite	106,4	98,0	115,4	-0,5	-1,8	0,9	0,514	0,023
A77-130	Corona	J2	125	Maiolica	Calcite	107,6	106,0	109,3	1,4	1,2	1,7	0,511	0,004
A77-40	Corona	J1	125	Maiolica	Calcite	55,9	39,9	74,7	-1,1	-3,9	1,9	0,608	0,000
A120	Subasio	J2	145	Scaglia Rossa	Calcite	71,7	71,7	71,7	-5,2	-5,2	-5,1	0,574	0,000
A28	Subasio	J1	106	Massiccio	Calcite	119,1	114,8	123,6	11,3	10,7	12,0	0,495	0,011
SUB15	Subasio	F1	77	Scaglia Cinerea	Calcite	78,3	71,7	85,3	8,4	7,4	9,5	0,561	0,022
SUB17	Subasio	F1	77	Scaglia Cinerea	Calcite	140,9	122,9	161,8	16,1	14,0	18,2	0,468	0,032
SUB30	Subasio	F1	81	Scaglia Cinerea	Calcite	104,4	100,1	108,9	11,4	10,8	12,1	0,516	0,012
A52	Nero	J1	115	Maiolica	Calcite	34,7	33,9	35,5	6,8	6,6	7,0	0,662	0,004
A56	Nero	J1	118	Scaglia Rossa	Calcite	27,2	15,9	39,9	2,7	0,3	5,2	0,685	0,052
A29	San Viccino	J1	108	Scaglia Rossa	Calcite	47,3	42,5	52,4	3,0	1,9	4,0	0,628	0,021
A39	San Viccino	J2	109	Scaglia Rossa	Calcite	74,5	64,7	85,2	7,2	5,6	8,8	0,568	0,035
FAB3	San Viccino	F2	50	Langhian Flysch	Calcite	36,5	32,8	40,3	2,5	1,7	3,3	0,658	0,018
FAB6	San Viccino	F2	50	Langhian Flysch	Calcite	70,3	63,7	77,4	8,3	7,1	9,4	0,576	0,024
A59	Catria	J1	119	Maiolica	Calcite	44,3	40,7	48,0	8,6	7,8	9,3	0,637	0,013
A65	Catria	J2	122	Massiccio	Calcite	59,0	49,2	69,7	11,1	8,9	13,4	0,601	0,032
CON6	Conero	J1	68	Scaglia Rossa	Calcite	41,6	30,7	53,8	5,8	3,4	8,3	0,643	0,044

1200

1201